Energy balance in quasi-Lagrangian Riemann-based SPH schemes

J. Michel[a,b], M. Antuono[a,*], G. Oger[b], S. Marrone[a]

[a] *CNR-INM, Institute of Marine Engineering, Rome, Italy*
[b] *Ecole Centrale Nantes, LHEEA research department (ECN and CNRS), Nantes, France*

Abstract

The Smoothed Particle Hydrodynamics (SPH) method suffers from the presence of irregular particle distributions inherent in its Lagrangian nature. A way to circumvent this problem is to consider a quasi-Lagrangian SPH scheme and use a Particle Shifting Technique (PST). In this framework, we include an approximate Riemann solver to represent the particle interaction and obtain two different quasi-Lagrangian Riemann-based SPH schemes: one is a mass-constant SPH model whereas the other is derived from an ALE formalism. These schemes are examined and validated by focusing on their energy balance. In particular, the energy contribution provided by the terms associated to Riemann solver and PST is studied from both a theoretical and numerical point of view. The consistency and the diffusive properties of these energy terms are investigated on test cases involving confined and free-surface flows. Albeit the investigation is performed for a specific Riemann solver and PST, the proposed methodology can be easily extended to other formulations.
© 2023 Elsevier B.V. All rights reserved.

1. Introduction

In fluid simulations characterized by mixing and large deformations the Smoothed Particle Hydrodynamics (SPH) method may exhibit an irregular distribution of particles. This phenomenon is caused by the Lagrangian nature of the scheme which induces the particles to align along the flow trajectories, and leads to the deterioration of the kernel interpolation and of the simulation itself. To circumvent this problem, it is currently a common practice to use a Particle Shifting Technique (PST) to rearrange dynamically the particles distribution and reduce the particle disorder, at the price of the loss of the Lagrangian character of the scheme (see e.g. [1–4]). Historically, the first PST was introduced in SPH by Monaghan [1], the so-called XSPH method, to update the particle positions exclusively, *i.e.* without any modification to the continuity and momentum equations. The use of a PST only in the advective equation was then employed along with other regularization techniques as, for example, in Sun et al. [4] through the introduction of a diffusive term in the continuity equation, or by means of Riemann terms, *e.g.* in the particle refinement method by Chiron et al. [5]. In weakly-compressible SPH methods, however, it has been shown that this approach can lead to adverse effects, such as deviations of the pressure field from the mean level in confined flows

---

* Corresponding author.
  E-mail address: matteo.antuono@cnr.it (M. Antuono).

or large variations of the volume occupied by the fluid in violent sloshing motions [6–8]. These effects seem to be independent from the regularization technique at hand [7]. To overcome this issue, alternative and theoretically more consistent approaches have been proposed to deal with a PST: the Arbitrary Lagrangian Eulerian (ALE) formalism [3,9,10] and its variants [6,10]. Although a perfect SPH-ALE scheme should have the property of being reducible to either purely Lagrangian or Eulerian SPH schemes (*i.e.* no mass exchanges in Lagrangian framework and no volume variation in Eulerian representation), this property is complex to obtain in practice, due to the necessary presence of regularization terms.

The first SPH scheme based on an ALE formalism was derived by Vila [9]. While the Eulerian SPH formulation is recovered from the Vila's scheme, the purely Lagrangian SPH formulation is not. This is due to the presence of non-zero fluxes in the mass equation (even without PST) which are not expected in a Lagrangian scheme. Notwithstanding this issue, the Vila's scheme has been widely validated, firstly in its Lagrangian version by Marongiu et al. [11] and Koukouvinis et al. [12], and secondly with the introduction of a PST velocity by Oger et al. [3]. More recently, Antuono et al. [10] derived an SPH scheme with ALE formalism, *i.e.* the δ-ALE-SPH, that shares several similarities with the model of Oger et al. [3]. Differently from the latter work, however, diffusive terms borrowed from the δ-SPH scheme were used instead of Riemann terms. Incidentally, we observe that a mass-constant variant of the δ-ALE-SPH was proposed in Antuono et al. [10] which is equivalent to the δ^+-SPH method of [6]. This suggests a close relation between the ALE approach and the consistent inclusion of PST in SPH models described in [6]. In the present work we refer to the last two classes of schemes as "quasi-Lagrangian" schemes.

In any case, whereas the δ-SPH and its variants (namely, δ-ALE-SPH and δ^+-SPH) have received an increasing attention on the role played by the diffusive terms in the energy balance, this kind of analysis still lacks for Riemann-SPH schemes and quasi-Lagrangian schemes in general. The aim of the present work is, therefore, to fill this gap by studying two different quasi-Lagrangian schemes with Riemann solver and PST. In the ALE framework, we select the scheme in [10] and replace the diffusive terms with Riemann terms obtained following Parshikov & Medin [13]. The scheme of Antuono et al. [10] is preferred to the Vila's scheme since the Lagrangian, Riemann and PST parts are well separated, facilitating the derivation of their related energy contributions. As a second scheme, we consider the δ^+-SPH method in [6] and, similarly to what described previously, the diffusive terms are replaced by the Riemann terms.

From a physical point of view, the evaluation of the energy budget provides useful information about a given phenomenon. As an example, the knowledge of the amount of energy dissipated by the fluid is crucial to study the damping effect of a sloshing flow inside a tank (see, *e.g.*, [14,15]). From a numerical point of view, it is important to quantify the numerical energy dissipated by the scheme itself, a topic widely discussed during the last decade in the SPH community [16–21]. In the present work we follow the approach described in Antuono et al. [16] to derive the energy balance when a Riemann solver is used. In comparison to that work, here the procedure is much more complex because of the presence of the PST terms inside the continuity and momentum equations. To the authors' knowledge this is the first attempt to perform a detailed study of the energy balance when the PST terms are present. With respect to this, Table 1 provides a quick look at the works in the literature where the analysis of the energy balance is used. About the specific PST law chosen in this work, we consider the formula proposed in [22] with an improvement to make it applicable in the presence of fluid impacts.

Finally, the paper is organized as follows. The two quasi-Lagrangian schemes studied in the present paper are introduced in Section 2 and their properties are described. Section 3 is dedicated to the derivation of the energy balance, in addition to an in-depth analysis of its different components. Finally, the validation and discussion is performed in Section 4. The details of the derivation of the energy balance for the quasi-Lagrangian schemes and other complex developments are reported in Appendix. Due to the large number of energy terms appearing in this paper, solid boundaries are excluded from the study.

2. Two quasi-Lagrangian SPH schemes with Riemann solver

In this section we describe the structure of the quasi-Lagrangian SPH schemes with the inclusion of an approximate Riemann-solver. The idea at the basis of a quasi-Lagrangian SPH scheme is to add a small perturbation velocity $\delta\boldsymbol{u}_i$ to the Lagrangian velocity $\boldsymbol{u}_i$ in order to recover an isotropic particle distribution in space. The perturbation velocity $\delta\boldsymbol{u}_i$ is obtained through a Particle Shifting Technique (PST) and, as a consequence, is

Table 1
Summary of the works regarding the energy balance.

	Energy terms used to **study physical phenomena**	Energy terms used for **validation of SPH schemes**	Detailed study on the **energy balance**
Lagrangian	$-Sloshing$ 　Bulian et al. [23] 　Marsh et al. [24] 　Bouscasse et al. [14] $-Wave\ breaking$ 　Marrone et al. [25] 　Wei & Dalrymple [26] $-Wave\ propagation$ 　Meringolo et al. [20] $-Liquid\ impact$ 　Marrone et al. [27]	$-\delta\text{-}SPH$ 　Antuono et al. [28] 　Hammani et al. [29] $-Riemann-SPH$ 　Green et al. [30] 　Zhang et al. [31] [32] 　Meng et al. [33] [34] $-MPS/ISPH$ 　Khayyer et al. [35] $-FSI$ 　Li et al. [36] 　Hermange et al. [19]	$-\delta\text{-}SPH$ 　Antuono et al. [16] 　Cercos-Pita et al. [17] 　Cercos-Pita et al. [18] 　Meringolo et al. [37] $-Riemann-SPH$ 　Cercos-Pita et al. [17] 　(only theoretically) 　Collé et al. [38] 　(only theoretically)
Lagrangian + PST in advection equation		$-\delta\text{-}SPH$ 　Sun et al. [4] 　Michel et al. [22] 　Wang et al. [39] $-Riemann-SPH$ 　Michel et al. [22] 　Meng et al. [33] $-MPS/ISPH$ 　Khayyer et al. [21] $-Surface\ tension\ model$ 　Vergnaud et al. [40]	Sun et al. [4] ($\delta^{+}-$SPH)
Quasi-Lagrangian	$-Sloshing$ 　Marrone et al. [41]	$-Riemann-SPH$ 　Oger et al. [3] 　Collé et al. [38] 　Michel et al. [22] 　Vergnaud et al. [42] $-\delta\text{-}SPH$ 　Sun et al. [6] 　Antuono et al. [43]	

called PST velocity. In this framework, the Arbitrary-Lagrangian–Eulerian formulation (ALE) of the Navier–Stokes equations is particularly suitable, since $\delta\boldsymbol{u}_i$ appears explicitly within the continuity and momentum equations [3,10]. The first SPH scheme described in the present work belongs to the above class of solvers. Conversely, the second quasi-Lagrangian SPH scheme is built on the work of Sun et al. [6], in which the Navier–Stokes equations are rearranged by using a material derivative based on the advection velocity $\boldsymbol{u}_i + \delta\boldsymbol{u}_i$.

In both schemes the fluid is assumed to be weakly-compressible and barotropic. This means that there exists a state function relating the pressure P and the density field ρ. Since the density variations are assumed to be small, a linear equation of state is used, namely:

$$P = c_0^2 (\rho - \rho_0) + P_b,\tag{1}$$

where c_0 and ρ_0 are the nominal sound speed and density respectively, and P_b a possible background pressure. The flow is assumed to be weakly-compressible when density variations are small. In practice, density variations smaller than 1% are ensured by satisfying the following condition:

$$c_0 \geq 10 \max\left(U_{max}, \sqrt{(\Delta p)_{max}/\rho} \right)\tag{2}$$

where U_{max} and $(\Delta p)_{max}$ are respectively the maximum fluid velocity and the maximum pressure variation (with respect to the pressure at the free-surface) expected in the fluid domain (see *e.g.* [25]). The background pressure is usually set to zero, except in Section 4.1.1 where an analysis on its influence on the energy balance is provided.

2.1. Quasi-Lagrangian scheme from the ALE framework

The semi-discrete form of the Navier–Stokes equations for a weakly-compressible fluid in a generic ALE framework reads:

$$
\begin{aligned}
\frac{d\boldsymbol{x}_i}{dt} &= \boldsymbol{u}_i & &+ \boldsymbol{\delta u}_i \\
\frac{dV_i}{dt} &= V_i \langle \mathrm{div}(\boldsymbol{u}_i) \rangle & &+ V_i \langle \mathrm{div}(\boldsymbol{\delta u}_i) \rangle \\
\frac{d(\rho_i V_i)}{dt} &= & &+ V_i \langle \mathrm{div}(\rho_i \boldsymbol{\delta u}_i) \rangle \\
\frac{d(\rho_i V_i \boldsymbol{u}_i)}{dt} &= - V_i \langle \boldsymbol{\nabla} P_i \rangle + \rho_i V_i \boldsymbol{f}_i & &+ V_i \langle \mathrm{div}(\mathbb{T}_i^{\nu}) \rangle \quad + V_i \langle \mathrm{div}(\rho_i \boldsymbol{u}_i \otimes \boldsymbol{\delta u}_i) \rangle
\end{aligned}
\tag{3}
$$

where $\boldsymbol{x}_i$, $\boldsymbol{u}_i$, V_i, ρ_i are the position, velocity, volume and density associated to the particle i while $\mathbb{T}_i^{\nu}$ and $\boldsymbol{f}_i$ are the viscous stress tensor and the volume force. The spatial differential operators appearing in (3) are discretized using the same SPH approximation as in [10]:

$$
\begin{aligned}
\langle \mathrm{div}(\boldsymbol{u}_i) \rangle &= \sum_j (\boldsymbol{u}_j - \boldsymbol{u}_i) \cdot \boldsymbol{\nabla}_i W_{ij} V_j & \langle \mathrm{div}(\boldsymbol{\delta u}_i) \rangle &= \sum_j (\boldsymbol{\delta u}_j - \boldsymbol{\delta u}_i) \cdot \boldsymbol{\nabla}_i W_{ij} V_j \\
\langle \boldsymbol{\nabla} P_i \rangle &= \sum_j (P_i + P_j) \boldsymbol{\nabla}_i W_{ij} V_j & \langle \mathrm{div}(\rho_i \boldsymbol{\delta u}_i) \rangle &= \sum_j (\rho_i \boldsymbol{\delta u}_i + \rho_j \boldsymbol{\delta u}_j) \cdot \boldsymbol{\nabla}_i W_{ij} V_j \\
\langle \mathrm{div}(\mathbb{T}_i^{\nu}) \rangle &= \mu \sum_j \pi_{ij}^{\mu} \boldsymbol{\nabla}_i W_{ij} V_j & \langle \mathrm{div}(\rho_i \boldsymbol{u}_i \otimes \boldsymbol{\delta u}_i) \rangle &= \sum_j (\rho_i \boldsymbol{u}_i \otimes \boldsymbol{\delta u}_i + \rho_j \boldsymbol{u}_j \otimes \boldsymbol{\delta u}_j) \boldsymbol{\nabla}_i W_{ij} V_j
\end{aligned}
\tag{4}
$$

where W is the kernel (the $\mathcal{C}^2$ Wendland kernel [44] is used throughout this paper). Since the scheme is centred in space and explicit in time, some kind of stabilization is needed to reduce the occurrence of spurious high-frequency noise. In particular a Riemann solver is used in the present work. Consequently, the first quasi-Lagrangian scheme studied in this paper reads:

$\boxed{QL\text{-}ALE\,scheme}$

$$
\begin{aligned}
\frac{d\boldsymbol{x}_i}{dt} &= & \boldsymbol{u}_i & & & + & & \boldsymbol{\delta u}_i \\
\frac{dV_i}{dt} &= & V_i \sum_j (\boldsymbol{u}_j - \boldsymbol{u}_i) \cdot \boldsymbol{\nabla}_i W_{ij} V_j & & + \; \Theta_{i,Rie}^{V} & & & +V_i \sum_j (\boldsymbol{\delta u}_j - \boldsymbol{\delta u}_i) \cdot \boldsymbol{\nabla}_i W_{ij} V_j \\
\frac{d(V_i \rho_i)}{dt} &= & 0 & & + & & & +V_i \sum_j (\rho_i \boldsymbol{\delta u}_i + \rho_j \boldsymbol{\delta u}_j) \cdot \boldsymbol{\nabla}_i W_{ij} V_j \\
\frac{d(V_i \rho_i \boldsymbol{u}_i)}{dt} &= & \underbrace{V_i \rho_i \boldsymbol{f}_i - V_i \sum_j (P_i + P_j)\boldsymbol{\nabla}_i W_{ij} V_j}_{\text{Lagrangian part}} + & \underbrace{\Theta_{i,Rie}^{V \rho \boldsymbol{u}}}_{\text{Riemann}} + & \underbrace{\boldsymbol{\Pi}_i^{\mu}}_{\text{Viscosity}} & & & +\underbrace{V_i \sum_j (\rho_i \boldsymbol{u}_i \otimes \boldsymbol{\delta u}_i + \rho_j \boldsymbol{u}_j \otimes \boldsymbol{\delta u}_j) \boldsymbol{\nabla}_i W_{ij} V_j}_{\text{PST part}}
\end{aligned}
\tag{5}
$$

where $\boldsymbol{\Pi}_i^{\mu} = V_i \langle \mathrm{div}(\mathbb{T}_i^{\nu}) \rangle = V_i \mu \sum_j \pi_{ij}^{\mu} \boldsymbol{\nabla}_i W_{ij} \; V_j$, μ is the dynamic viscosity and

$$
\pi_{ij}^{\mu} = 2(D+2) \frac{(\boldsymbol{u}_j - \boldsymbol{u}_i) \cdot (\boldsymbol{x}_j - \boldsymbol{x}_i)}{\|\boldsymbol{x}_j - \boldsymbol{x}_i\|^2} \quad \text{with } D \text{ the spatial dimension.}
\tag{6}
$$

$\Theta_{i,Rie}^{V}$ and $\boldsymbol{\Theta}_{i,Rie}^{V \rho \boldsymbol{u}}$ stand for the Riemann terms in the volume and momentum equations respectively. They are detailed in Section 2.3. Thanks to the anti-symmetric structure of the SPH operators for $V_i \langle \mathrm{div}(\rho_i \boldsymbol{\delta u}_i) \rangle$, $V_i \langle \boldsymbol{\nabla} P_i \rangle$, $V_i \langle \mathrm{div}(\rho_i \boldsymbol{u}_i \otimes \boldsymbol{\delta u}_i) \rangle$ and $\boldsymbol{\Theta}_{i,Rie}^{V \rho \boldsymbol{u}}$ both the total mass and the linear momentum are conserved (see also Section 2.3 for details). However, the angular momentum is not strictly conserved [10].

In practical simulations, the use of a quasi-Lagrangian SPH scheme in the ALE framework without any regularization mechanism can lead to large variations of the volume/mass of isolated particles. To address this issue, a diffusive term was added in the mass equation in [10], built via a Laplacian operator. Another possibility to overcome this issue was developed by Sun et al. [6] where, similarly to Adami et al. [45], an alternative material

derivative was introduced, leading to a quasi-Lagrangian SPH scheme in which: (i) particle masses are constant, (ii) the PST is taken into account within the continuity and momentum equations.

Since the use of Riemann solver is in essence different to the use of explicit diffusive terms, it is not trivial to modify the mass equation by introducing a diffusive term in a manner compatible with the Riemann solver. By contrast, adapting the quasi-Lagrangian scheme of Sun et al. [6] to the use of Riemann solver is straightforward, as detailed in the following section.

2.2. Quasi-Lagrangian scheme with constant masses

As originally pointed by Adami et al. [45], when the particles move with an advection velocity which differs from the Lagrangian velocity, the material derivative has to be modified accordingly. As shown in Sun et al. [6], if the advection velocity is $\boldsymbol{u} + \boldsymbol{\delta u}$, then the following relation holds true:

$$\frac{d(\bullet)}{dt} = \frac{D(\bullet)}{Dt} + \boldsymbol{\nabla}(\bullet) \cdot \boldsymbol{\delta u}, \quad \text{where } \frac{D(\bullet)}{Dt} \text{ is the Lagrangian material derivative.} \tag{7}$$

Differently from [45] (where the Eq. (7) was applied to the momentum equation exclusively while the density was computed through a summation $\rho_i = m_i \sum_j W_{ij}$ where m_i indicates the particle mass), in Sun et al. [6] the modified material derivative was applied to both the continuity and momentum equations, leading to the following semi-discrete form:

$$
\begin{aligned}
\frac{d\boldsymbol{x}_i}{dt} &= \boldsymbol{u}_i &&+ \boldsymbol{\delta u}_i \\
\frac{dV_i}{dt} &= V_i \langle \mathrm{div}(\boldsymbol{u}_i) \rangle &&+ V_i \langle \mathrm{div}(\boldsymbol{\delta u}_i) \rangle - \frac{V_i}{\rho_i} \langle \mathrm{div}(\rho_i \boldsymbol{\delta u}_i) \rangle \\
\frac{d(\rho_i V_i)}{dt} &= 0 \\
\frac{d(V_i \rho_i \boldsymbol{u}_i)}{dt} &= -V_i \langle \boldsymbol{\nabla} P_i \rangle + \rho_i V_i \boldsymbol{f}_i \quad + V_i \langle \mathrm{div}(\mathbb{T}_i^\nu) \rangle \quad + V_i \langle \mathrm{div}(\rho_i \boldsymbol{u}_i \otimes \boldsymbol{\delta u}_i) \rangle - V_i \boldsymbol{u}_i \langle \mathrm{div}(\rho_i \boldsymbol{\delta u}_i) \rangle
\end{aligned}
\tag{8}
$$

where, differently from Sun et al. [6], the equations are written here in terms of $\frac{dV_i}{dt}$ and $\frac{d(V_i \rho_i \boldsymbol{u}_i)}{dt}$ in analogy with the ALE system (3). Finally, using the spatial differential operators in (4), the following scheme is obtained:

$\boxed{QL\text{-}MassCons \ scheme}$

$$
\begin{aligned}
\frac{d\boldsymbol{x}_i}{dt} &= &&\boldsymbol{u}_i &&+ &&\boldsymbol{\delta u}_i \\
\frac{dV_i}{dt} &= V_i \sum_j (\boldsymbol{u}_j - \boldsymbol{u}_i) \cdot \boldsymbol{\nabla}_i W_{ij} V_j &&+ \quad \Theta_{i,Rie}^V &&+ V_i \sum_j \left[(\boldsymbol{\delta u}_j - \boldsymbol{\delta u}_i) - \frac{\rho_i \boldsymbol{\delta u}_i + \rho_j \boldsymbol{\delta u}_j}{\rho_i} \right] \cdot \boldsymbol{\nabla}_i W_{ij} V_j \\
\frac{d(V_i \rho_i)}{dt} &= &&0 \\
\frac{d(V_i \rho_i \boldsymbol{u}_i)}{dt} &= V_i \rho_i \boldsymbol{f}_i - V_i \sum_j (P_i + P_j) \boldsymbol{\nabla}_i W_{ij} V_j + \Theta_{i,Rie}^{V\rho\boldsymbol{u}} &&+ \boldsymbol{\Pi}_i^\mu + V_i \sum_j (\rho_i \boldsymbol{u}_i \otimes \boldsymbol{\delta u}_i + \rho_j \boldsymbol{u}_j \otimes \boldsymbol{\delta u}_j) \boldsymbol{\nabla}_i W_{ij} V_j
\end{aligned}
\tag{9}
$$

$$\underbrace{\phantom{V_i \rho_i \boldsymbol{f}_i - V_i \sum_j (P_i + P_j) \boldsymbol{\nabla}_i W_{ij} V_j}}_{\text{Lagrangian part}} \quad \underbrace{\phantom{\Theta_{i,Rie}^{V\rho\boldsymbol{u}}}}_{\substack{\text{Riemann Viscosity}}} \quad \underbrace{\phantom{V_i \sum_j (\rho_i \boldsymbol{u}_i \otimes \boldsymbol{\delta u}_i + \rho_j \boldsymbol{u}_j \otimes \boldsymbol{\delta u}_j)}}_{\text{PST part}}$$

---

where $\Theta_{i,Rie}^V$, $\boldsymbol{\Theta}_{i,Rie}^{V\rho\boldsymbol{u}}$, and $\boldsymbol{\Pi}_i^\mu$ are identical to those in the *QL-ALE* scheme (5). Note that, similarly to [6,45], the term $V_i \boldsymbol{u}_i \langle \mathrm{div}(\rho_i \boldsymbol{\delta u}_i) \rangle$ appearing in the momentum equation of (8) is not discretized, since it is negligible in comparison to the other terms. This simplification, though small, leads to the loss of the Galilean invariance of the scheme. In any case, this aspect is not inspected here and is left to future studies. Incidentally, we observe that, similarly to the *QL-ALE* model, the *QL-MassCons* scheme does not strictly preserve angular momentum while it preserves mass and linear momentum.

2.3. Riemann solvers in SPH

The use of Riemann solvers in the SPH context is commonly discussed in the literature (see e.g. [3,12,30,31,46–49]). It consists of three main parts: (i) the introduction of the Riemann problem solutions within

the SPH scheme, (ii) the reconstruction of the left and right states ϕ_L and ϕ_R, and (iii) the choice of the specific Riemann solver.

2.3.1. How to introduce Riemann problem solutions within an SPH scheme

Vila [9] and Parshikov [50] (see also Parshikov & Medin [13]) presented almost simultaneously two different Riemann-based SPH schemes. Vila [9] introduced this formalism through mass and momentum fluxes within an ALE framework. Because of this structure, this technique implies mass exchanges even in its Lagrangian version (i.e. even when $\delta u = 0$). Conversely, a purely Lagrangian SPH scheme with no mass fluxes was adopted by Parshikov [50]. Furthermore, in the Vila's formalism, a strict separation of the Riemann and PST parts (as done for the *QL-ALE* and *QL-MassCons* schemes in Sections 2.1 and 2.2) is hard to obtain, while it comes naturally when the Parshikov technique is used. For these reasons, in the present paper the latter technique is preferred. It consists in isolating the arithmetic means $(u_i + u_j)/2$ and $(P_i + P_j)/2$ inside the divergence and gradient operators respectively and in replacing them by the Riemann problem solutions u_E and P_E, as:

$$\sum_j (u_j - u_i) \cdot \nabla_i W_{ij} V_j = \sum_j 2 \left(\frac{u_j + u_i}{2} - u_i \right) \cdot \nabla_i W_{ij} V_j \approx \sum_j 2 (u_E - u_i) \cdot \nabla_i W_{ij} V_j, \tag{10}$$

$$\sum_j (P_i + P_j) \nabla_i W_{ij} V_j = \sum_j 2 \left(\frac{P_i + P_j}{2} \right) \nabla_i W_{ij} V_j \approx \sum_j 2 P_E \nabla_i W_{ij} V_j. \tag{11}$$

From the expressions above, it comes

$$\Theta_{i,Rie}^{V} = V_i \sum_j \boldsymbol{\theta}_{ij,Rie}^{V} \cdot \nabla_i W_{ij} V_j \quad \text{with} \quad \boldsymbol{\theta}_{ij,Rie}^{V} = 2 u_E - (u_i + u_j) \tag{12}$$

and

$$\boldsymbol{\Theta}_{i,Rie}^{V\rho u} = -V_i \sum_j \theta_{ij,Rie}^{V\rho u} \nabla_i W_{ij} V_j \quad \text{with} \quad \theta_{ij,Rie}^{V\rho u} = 2 P_E - (P_i + P_j) \tag{13}$$

as introduced in Eqs. (5) and (9).

2.3.2. Left and right states of the Riemann problem

Among the large number of reconstruction schemes available in the literature, the method chosen in the present study is widely inspired from [51], where the work initially proposed by Van Leer [52] was adapted to the SPH method. Precisely, supposing that the $i - j$ interface is located at $x_{ij} = 0.5(x_i + x_j)$, the determination of the left state ϕ_L of the Riemann problem first consists in computing two slopes $\Delta\phi_1$ and $\Delta\phi_2$:

$$\Delta\phi_1 = \frac{\phi_j - \phi_i}{\|x_j - x_i\|} \quad \text{and} \quad \Delta\phi_2 = \nabla^{\mathcal{L}} \phi_i \frac{x_j - x_i}{\|x_j - x_i\|}, \tag{14}$$

where

$$\nabla^{\mathcal{L}} \phi_i = \mathbb{L}_i \sum_j (\phi_j - \phi_i) \nabla_i W_{ij} V_j \quad \text{with} \quad \mathbb{L}_i = \left[\sum_j (x_j - x_i) \otimes \nabla_i W_{ij} V_j \right]^{-1} \tag{15}$$

Then, the following slope limiter is used:

$$\Delta\phi = \begin{cases} \dfrac{2\Delta\phi_1 \Delta\phi_2}{\Delta\phi_1 + \Delta\phi_2} & \text{if} \quad \Delta\phi_2 \Delta\phi_1 > 0 \\ 0 & \text{otherwise.} \end{cases} \tag{16}$$

Finally, the left state is defined as:

$$\phi_L = \phi_i + 0.5\Delta\phi \|x_j - x_i\|, \tag{17}$$

and a similar procedure is used to compute the right state ϕ_R.

2.3.3. Riemann solver

Finally, the numerical flux within the particle interaction is obtained through a specific Riemann solver which can be exact or approximate. In the present paper, the approximate Riemann solver usually named Primitive Variable Riemann Solver (PVRS) (see *e.g.* [53]) is used, since it provides results that are very close to those predicted by the exact Riemann solver, but at a lower computational cost. Note that in the present work, the considered primitive variables are ρ and $\boldsymbol{u}$, the related pressure P being determined through Eq. (1). Since a constant speed of sound is imposed by (1), *i.e.* $c_L = c_R = c_0$, the Riemann problem solutions read:

$$\boldsymbol{u}_E = \frac{\rho_R c_0 u_R + \rho_L c_0 u_L - P_R + P_L}{\rho_R c_0 + \rho_L c_0} \frac{\boldsymbol{x}_j - \boldsymbol{x}_i}{\|\boldsymbol{x}_j - \boldsymbol{x}_i\|}, \tag{18}$$

$$P_E = \frac{\rho_R P_L + \rho_L P_R - \rho_R \rho_L c_0 \left(u_R - u_L\right)}{\rho_R + \rho_L}. \tag{19}$$

Assuming the fluid to be weakly-compressible and the flow fields and the particle distribution to be regular, the above expressions allow for an analysis of the convergence of the Riemann terms. As shown in Appendix D, we prove the following leading-order contributions:

$$\frac{\Theta_{i,Rie}^{V}}{V_i} = -\frac{3}{8} R^2 \alpha \, \Delta \left(\nabla \cdot \boldsymbol{u}\right) + \frac{1}{c_0 \rho_0} \frac{R^3}{16} \beta \, \Delta^2 P + \mathcal{O}\left(R^4\right),$$

$$\frac{\Theta_{i,Rie}^{V \rho \boldsymbol{u}}}{V_i} = +\frac{3}{8} R^2 \alpha \, \nabla \left(\Delta P\right) - \rho_0 c_0 \frac{R^3}{120} \gamma \left[\Delta^2 \boldsymbol{u} + 4 \nabla \left(\Delta \left(\nabla \cdot \boldsymbol{u}\right)\right)\right] + \mathcal{O}\left(R^4\right),$$

where α, β and γ are positive dimensionless constant (defined in the Appendix D) and R is the radius of the kernel function. The above expressions guarantee that, under the hypothesis discussed above, both the Riemann terms behave as diffusive terms, and are $\mathcal{O}(R^2)$. This suggests some analogies between the inclusion of Riemann solvers in the SPH framework and the use of the diffusive term of the δ-SPH [28], as already observed in Green et al. [30]. In any case, this topic is left to future studies.

2.4. Particle Shifting Technique

In the present work the PST derived in [22] is used. This choice is motivated by the fact that the related shifting velocity satisfies the condition $\boldsymbol{\delta u}_i = \mathcal{O}(\Delta x)$. Nevertheless, two modifications are brought with respect to [22]. The first modification regards the computation of the vector pointing towards the zone of low concentration of particles, hereinafter denoted by $-\nabla C_i$, in the region close to the free-surface. In [22], a constant kernel radius was used to compute this vector in all the fluid domain, implying that in the free-surface region it was always pointing outside the free-surface. This feature becomes particularly problematic when long duration simulations are considered, as described in [39]. To avoid this issue, a variable kernel radius is used in the present paper to compute $-\nabla C_i$, in analogy to that proposed in [39]. The second modification is about the limitation of the influence of the PST onto the variation of ρ_i. As shown in Appendix C, the leading order terms of the density equation for both the *QL-ALE* and *QL-MassCons* schemes are:

$$\frac{d\rho_i}{dt} \approx \underbrace{-\rho_i \sum_j \left(\boldsymbol{u}_j - \boldsymbol{u}_i\right) \cdot \nabla_i W_{ij} \, V_j}_{\text{Lagrangian part}} + \underbrace{2\rho_i \boldsymbol{\delta u}_i \cdot \nabla \Gamma_i}_{\text{PST part}} . \tag{20}$$

The additional control is added to limit the term $\boldsymbol{\delta u}_i \cdot \nabla \Gamma_i$ and, therefore, the influence of the PST on the density variations. This limitation is particularly relevant during fluid impacts, where both $\boldsymbol{\delta u}_i$ and $\nabla \Gamma_i$ can assume large values (see, for example, [54]).

It is important to highlight that the above-mentioned modifications preserve the properties of the PST proposed in [22], namely the consistency, the Galilean invariance, the local rotation invariance and the locality of the PST (*i.e.* the fact that $\boldsymbol{\delta u}_i$ is computed exclusively through local quantities, and therefore it is independent of the global fluid flow solution). Below, the PST velocity used in this paper is detailed.

The first stage of many PSTs of the literature (see *e.g.* [2,3,6,22,39]) consists in computing a non-dimensional vector, say $\boldsymbol{J}_i$, pointing towards zones of low concentration of particles. In the present paper, such a vector is
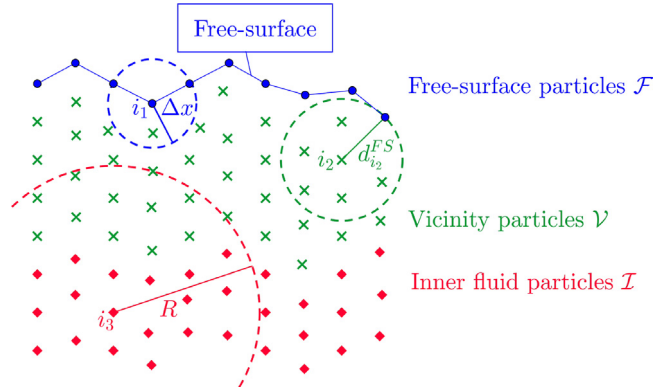
Fig. 1. Radius used to compute the vector pointing towards zones of low concentration of particles, depending on its position regarding the free-surface. Within the free-surface region – defined as the union of the free-surface particles (blue particles) and the particles inside the kernel support of at least one free-surface particle (green particles) –, the radius is set as the distance between the particle of interest and the free-surface (see *e.g.* i_2); if this distance is smaller than Δx, the radius is set to Δx (see *e.g.* i_1). For inner fluid particles (red particles), the radius is set to R (see *e.g.* i_3). (For interpretation of the references to color in this figure legend, the reader is referred to the web version of this article.)

computed as:

$$\boldsymbol{J}_i = -R_i \left(R_i/\Delta x\right)^3 \boldsymbol{\nabla} C_i \quad \text{where} \quad \boldsymbol{\nabla} C_i = \sum_{j \in \mathcal{D}_i^*} \left[1 + 0.2 \left(\frac{W_{ij}^*}{W^*(\Delta x R_i/R)} \right)^4 \right] \boldsymbol{\nabla}_i W_{ij}^* V_j \tag{21}$$

and R_i is the variable kernel radius. In particular, $R_i = \min\left(R, \max\left(\Delta x, d_i^{FS}\right)\right)$ where Δx is the initial particle distance, d_i^{FS} is the distance between particle i and its closest free-surface particle (detected through the algorithm in [55]) and W_i^* is the corresponding kernel function of support $\mathcal{D}_i^*$, as sketched in Fig. 1. The coefficient $(R_i/\Delta x)^3$ allows for counter-balancing the leading-order term appearing in the truncation error of $\boldsymbol{\nabla} C_i$, and, since $R_i = \Delta x$ for the particles located at the free-surface, it is consistent with the theoretical results obtained for an half-filled kernel support [22].

In order to ensure the kinematic free-surface condition, $\boldsymbol{J}_i$ has to be projected tangentially to the free-surface region. Following [22], only the tangential component is used for the free-surface particles and for vicinity particles such that $d_i^{FS} \leq R/2$. For vicinity particles for which $d_i^{FS} > R/2$, the normal component of $\boldsymbol{J}_i$ is progressively authorized, until the inner part of the fluid is reached for which $\boldsymbol{J}_i$ is taken as it is. This vector finally reads:

$$\boldsymbol{J}_i^\perp = \boldsymbol{J}_i - \sigma_i^\perp \left(\boldsymbol{J}_i \cdot \tilde{\boldsymbol{n}}_i\right) \tilde{\boldsymbol{n}}_i, \quad \text{with} \quad \sigma_i^\perp = \min\left[1, \max\left(0, \frac{d_i^{FS} - R}{R/2 - R}\right)\right]. \tag{22}$$

where $\tilde{\boldsymbol{n}}_i$ stands for the normal vector in the free-surface region. Remarkably, since $\delta \boldsymbol{u}_i \cdot \boldsymbol{\nabla} \Gamma_i \approx 0$ at the free-surface, the dynamic free-surface boundary condition is not altered by the PST contribution (see Eq. (20)).

The last step consists in deriving the PST velocity $\delta \boldsymbol{u}_i$. In [22], this is performed through:

$$\delta \boldsymbol{u}_i = \boldsymbol{J}_i^\perp \min\left(U_i^{char}; \frac{1}{2} \frac{R}{\Delta x} \frac{U_i^{char}}{\|\boldsymbol{J}_i^\perp\|} \right) \quad \text{where} \quad U_i^{char} = 0.5 \max_j \left(\left| (\boldsymbol{u}_j - \boldsymbol{u}_i) \cdot \frac{\boldsymbol{x}_j - \boldsymbol{x}_i}{\|\boldsymbol{x}_j - \boldsymbol{x}_i\|} \right| \right),$$

implying $\delta \boldsymbol{u}_i = \mathcal{O}(\Delta x)$, and, consequently, $\delta \boldsymbol{u}_i \cdot \boldsymbol{\nabla} \Gamma_i = \mathcal{O}(1)$ (see Appendix C). Since $|\delta \boldsymbol{u}_i \cdot \boldsymbol{\nabla} \Gamma_i|$ can assume large values an additional control is proposed to avoid large density variations as described in Eq. (20). Precisely, the variation of ρ_i due to the PST part during one time-step Δt is limited to $\epsilon \rho_i$ with $\epsilon \ll 0.01$. This leads to:

$$\Delta t |2\rho_i \delta \boldsymbol{u}_i \cdot \boldsymbol{\nabla} \Gamma_i| \leq \epsilon \rho_i \iff |\delta \boldsymbol{u}_i \cdot \boldsymbol{\nabla} \Gamma_i| \leq \frac{\epsilon}{2\Delta t}. \tag{23}$$

Finally, the PST used in the present paper reads:

$$\delta \boldsymbol{u}_i = \boldsymbol{J}_i^\perp \min\left[\min\left(U_i^{char}; \frac{1}{2} \frac{R}{\Delta x} \frac{U_i^{char}}{\|\boldsymbol{J}_i^\perp\|} \right), \frac{\epsilon}{2\Delta t |\boldsymbol{J}_i^\perp \cdot \boldsymbol{\nabla} \Gamma_i|} \right], \tag{24}$$

where the last term in the right hand side of Eq. (24) stands for the additional limitation with $\epsilon = 5.10^{-5}$ and $R/\Delta x = 4$ (unless otherwise specified). Accordingly to [22], $\delta\boldsymbol{u}_i$ is set to $\boldsymbol{0}$ for particles with a low numbers of neighbours (typically in a jet of fluid), since $\tilde{\boldsymbol{n}}_i$ is ill-computed in that case; the corresponding criteria is $\lambda_i < 0.4$ where λ_i is the minimum eigenvalues of the inverse of the renormalization matrix $\mathbb{L}_i$ (15).

2.5. Time integration

Both schemes are integrated in time through a 4th-order Runge–Kutta scheme, with the following CFL condition:

$$\Delta t = \min\left(CFL_h \frac{R}{c_0}, CFL_v \frac{R^2}{\nu}\right) \tag{25}$$

Preliminary analysis based on energy considerations led to $CFL_h = 0.5$ and $CFL_v = 0.025$ as reasonable values for the test cases under investigation.

3. Energy balance for the *QL-ALE* and *QL-MassCons* schemes

The present section is dedicated to the derivation of the energy balance for the two quasi-Lagrangian schemes introduced in Section 2. In the SPH literature a work in this sense was already performed by Antuono et al. [16] addressing a purely Lagrangian SPH scheme. The present work presents two major differences with respect to [16]: (i) Riemann solver is used instead of a numerical diffusion in the continuity equation, (ii) quasi-Lagrangian schemes are considered and, therefore, PST terms appear in the energy balance. Regarding the point (i), a key element is to make the Riemann terms explicit, as performed in Section 2. Then, the methodology derived in [16] is extended to the schemes under investigation in order to study the energy contributions coming from the Riemann solver and from the PST.

All the details on the derivation of the energy balance are reported in Appendices A and B, while in this section only the final results are reported. For the sake of simplicity, we only consider fluid–fluid interactions and neglect the presence of solid boundaries. Accordingly, we only consider benchmark cases without solid boundaries and postpone the study in presence of solid walls to future works.

The energy balance for the *QL-ALE* and *QL-MassCons* schemes reads:

$$\frac{d\mathcal{E}_k}{dt} + \frac{d\mathcal{E}_C}{dt} - \mathcal{P}_\mu - \mathcal{P}_{Rie} - \mathcal{P}_{\delta\boldsymbol{u}} - \mathcal{P}_f = 0 \tag{26}$$

where $\mathcal{E}_k$ and $\mathcal{E}_C$ are respectively the kinetic and compressible energies defined as:

$$\mathcal{E}_k = \frac{1}{2}\sum_i m_i \|\boldsymbol{u}_i\|^2 \tag{27}$$

$$\mathcal{E}_C = \sum_i m_i\, e_i \qquad \text{where} \quad e_i = \int_{\rho_0}^{\rho_i} \frac{P(s)}{s^2}\, ds \tag{28}$$

and $m_i = \rho_i V_i$ is the mass of the ith particle. Using Eq. (1), we obtain:

$$e_i = c_0^2 \log\left(\frac{\rho_i}{\rho_0}\right) - \frac{P_i}{\rho_i} + \frac{P_b}{\rho_0}. \tag{29}$$

The power term $\mathcal{P}_\mu$ is related to the viscous term (identical for the *QL-ALE* and *QL-MassCons* schemes) and reads:

$$\mathcal{P}_\mu = \frac{\mu}{2}\sum_i \sum_j \pi_{ij}^\mu \left(\boldsymbol{u}_i - \boldsymbol{u}_j\right) \cdot \nabla_i W_{ij} V_i V_j, \quad \text{with } \pi_{ij}^\mu \text{ defined in Eq. (6)} \tag{30}$$

As shown for example in [56], this term is purely dissipative. The power term $\mathcal{P}_{Rie} := \mathcal{P}_{Rie}^{cont} + \mathcal{P}_{Rie}^{mom}$ contains the contributions from the Riemann terms where

$$\mathcal{P}_{Rie}^{cont} = \frac{1}{2}\sum_i \sum_j \left(P_j - P_i\right)\boldsymbol{\theta}_{ij,Rie}^V \cdot \nabla_i W_{ij} V_i V_j \qquad \text{with } \boldsymbol{\theta}_{ij,Rie}^V \text{ defined in Eq. (12)} \tag{31}$$

$$\mathcal{P}_{Rie}^{mom} = \frac{1}{2} \sum_i \sum_j \theta_{ij,Rie}^{V\rho\boldsymbol{u}} (\boldsymbol{u}_i - \boldsymbol{u}_j) \cdot \boldsymbol{\nabla}_i W_{ij} V_i V_j \qquad \text{with } \theta_{ij,Rie}^{V\rho\boldsymbol{u}} \text{ defined in Eq. (13)} \tag{32}$$

This term is identical for the *QL-ALE* and *QL-MassCons* schemes. Finally, $\mathcal{P}_{\boldsymbol{\delta u}} := \mathcal{P}_{\boldsymbol{\delta u}}^{cont} + \mathcal{P}_{\boldsymbol{\delta u}}^{mom}$ is the power term related to the PST terms. This differs between the *QL-ALE* and *QL-MassCons* schemes. Specifically:

- for the *QL-ALE* scheme:

$$\mathcal{P}_{\boldsymbol{\delta u}}^{cont} = \frac{1}{2} \sum_i \sum_j \left[-(P_i + P_j) (\boldsymbol{\delta u}_j - \boldsymbol{\delta u}_i) \right] \cdot \boldsymbol{\nabla}_i W_{ij} V_i V_j + \mathcal{P}_{\boldsymbol{\delta u}}^{m,2} \tag{33}$$

$$\mathcal{P}_{\boldsymbol{\delta u}}^{mom} = \frac{1}{2} \sum_i \sum_j (\boldsymbol{u}_i - \boldsymbol{u}_j) \cdot \left[\left(\rho_i \boldsymbol{u}_i \otimes \boldsymbol{\delta u}_i + \rho_j \boldsymbol{u}_j \otimes \boldsymbol{\delta u}_j \right) \boldsymbol{\nabla}_i W_{ij} V_i V_j \right] + \mathcal{P}_{\boldsymbol{\delta u}}^{m,1} \tag{34}$$

where $\mathcal{P}_{\boldsymbol{\delta u}}^{m,2}$ and $\mathcal{P}_{\boldsymbol{\delta u}}^{m,1}$ come from the mass evolution equation of (5) and read:

$$\mathcal{P}_{\boldsymbol{\delta u}}^{m,1} = \frac{1}{4} \sum_i \sum_j \left(\|\boldsymbol{u}_j\|^2 - \|\boldsymbol{u}_i\|^2 \right) \left(\rho_i \boldsymbol{\delta u}_i + \rho_j \boldsymbol{\delta u}_j \right) \cdot \boldsymbol{\nabla}_i W_{ij} V_i V_j \tag{35}$$

$$\mathcal{P}_{\boldsymbol{\delta u}}^{m,2} = \frac{1}{2} \sum_i \sum_j c_0^2 \log \left(\frac{\rho_i}{\rho_j} \right) \left(\rho_i \boldsymbol{\delta u}_i + \rho_j \boldsymbol{\delta u}_j \right) \cdot \boldsymbol{\nabla}_i W_{ij} V_i V_j \tag{36}$$

- while for the *QL-MassCons* scheme:

$$\mathcal{P}_{\boldsymbol{\delta u}}^{cont} = \frac{1}{2} \sum_i \sum_j \left[-(P_i + P_j) (\boldsymbol{\delta u}_j - \boldsymbol{\delta u}_i) + \left(\frac{P_i}{\rho_i} - \frac{P_j}{\rho_j} \right) \left(\rho_i \boldsymbol{\delta u}_i + \rho_j \boldsymbol{\delta u}_j \right) \right] \cdot \boldsymbol{\nabla}_i W_{ij} V_i V_j \tag{37}$$

$$\mathcal{P}_{\boldsymbol{\delta u}}^{mom} = \frac{1}{2} \sum_i \sum_j (\boldsymbol{u}_i - \boldsymbol{u}_j) \cdot \left[\left(\rho_i \boldsymbol{u}_i \otimes \boldsymbol{\delta u}_i + \rho_j \boldsymbol{u}_j \otimes \boldsymbol{\delta u}_j \right) \boldsymbol{\nabla}_i W_{ij} V_i V_j \right] \tag{38}$$

Finally, $\mathcal{P}_f$ is the power of the external volume force $\boldsymbol{f}_i$, that is $\mathcal{P}_f = \sum_i m_i \boldsymbol{u}_i \cdot \boldsymbol{f}_i$. If $\boldsymbol{f}_i$ is a conservative force, the scheme admits a potential energy as below

$$\mathcal{E}_p = -\sum_i m_i \Phi_i \qquad \text{with} \qquad \boldsymbol{f}_i = \boldsymbol{\nabla} \Phi_i \tag{39}$$

In such a case, as shown in Appendix A, the energy balance (26) can be rewritten as:

$$\frac{d\mathcal{E}_k}{dt} + \frac{d\mathcal{E}_C}{dt} + \frac{d\mathcal{E}_p}{dt} = \mathcal{P}_\mu + \mathcal{P}_{Rie} + \mathcal{P}_{\boldsymbol{\delta u}} + \mathcal{P}_{\boldsymbol{\delta u}}^f \tag{40}$$

with

$$\mathcal{P}_{\boldsymbol{\delta u}}^f = -\sum_i m_i \boldsymbol{\delta u}_i \cdot \boldsymbol{f}_i - \sum_i \frac{dm_i}{dt} \Phi_i \tag{41}$$

where the first term on the right hand side of Eq. (41) represents the modification of the potential due to the arbitrary displacements induced by $\boldsymbol{\delta u}_i$, and the second term (only present with the *QL-ALE* scheme) represents the modification of the potential due to the mass variations induced by $\boldsymbol{\delta u}_i$.

From the above derivations it is possible to draw some general discussions about their diffusive nature and their consistency (in the sense that their contribution goes to zero when refining the spatial resolution). Regarding the Riemann term $\mathcal{P}_{Rie}$, the diffusive and consistency aspects of $\Theta_{i,Rie}^V$ and $\Theta_{i,Rie}^{V\rho\boldsymbol{u}}$ have been studied theoretically in Section 2.3 under hypotheses of flow field regularity. Nevertheless, during the flow evolution these hypotheses are not necessarily verified, and it is of paramount importance to check how $\mathcal{P}_{Rie}$ behaves. This is performed in Section 4.

As for $\mathcal{P}_{\boldsymbol{\delta u}}^{cont}$, some theoretical findings can be derived. As shown in Appendix C.2, for both the *QL-ALE* and *QL-MassCons* schemes the leading-order contribution is

$$\mathcal{P}_{\boldsymbol{\delta u}}^{cont} \approx 2 \sum_i V_i P_i \boldsymbol{\delta u}_i \cdot \boldsymbol{\nabla} \Gamma_i . \tag{42}$$

We observe that the consistency is strictly related to the consistency of δu_i itself. Since in the present paper δu_i is $\mathcal{O}(\Delta x)$, we expect $\mathcal{P}_{\delta u}^{cont} = \mathcal{O}(1)$, which is numerically confirmed in Section 4. The second aspect regards the existing link between the sign of the pressure field and the sign of $\mathcal{P}_{\delta u}^{cont}$. In fact, like many other PSTs in the literature (e.g. [2,3,6]), the one used in the present paper is based on the gradient of the particle concentration. Therefore, the vector δu_i is approximately parallel to $\nabla \Gamma_i$ and points in the opposite direction; this mainly happens when particle gaps occur, as for example during fluid impacts or at the core of high vorticity regions. This implies that the sign of $\delta u_i \cdot \nabla \Gamma_i$ is generally negative and, consequently, the sign of $\mathcal{P}_{\delta u}^{cont}$ essentially depends on the sign of the pressure field. In regions where the pressure field is positive, $\mathcal{P}_{\delta u}^{cont}$ is negative and, therefore, represents a dissipation. On the contrary, $\mathcal{P}_{\delta u}^{cont}$ becomes positive when the pressure is negative and represents a source of energy for the system. The link between dissipation/source of energy and the pressure sign is studied numerically in Section 4.3. Furthermore, $\mathcal{P}_{\delta u}^{cont}$ is not invariant by change of reference pressure. When a background pressure P_b is considered, a quantity $2P_b \sum_i V_i \delta u_i \cdot \nabla \Gamma_i$ adds to $\mathcal{P}_{\delta u}^{cont}$. This aspect is investigated numerically in Section 4.1.1. About the remaining components in Eq. (40), it is impossible to draw considerations *a priori* on their properties.

4. Validation/discussion

The present section is dedicated to the validation of the quasi-Lagrangian schemes described in the previous sections and to the analysis of the role of the different energy terms. Three test cases are considered here, namely (i) the Taylor–Green flow for a viscous fluid at $Re = 1000$ and for an inviscid fluid, (ii) a periodic inviscid oscillating drop under a conservative force field, and (iii) an impact of two patches of inviscid fluid. For each test case under investigation, the following analysis is performed. Firstly, both the *QL-ALE* and *QL-MassCons* schemes are validated with specific attention to the pressure field and the flow kinematics. The numerical solutions are shown for both the schemes only when significant differences are observed, the results obtained with the *QL-MassCons* scheme are reported otherwise. Then, the different components appearing in the energy balance are studied. Differently from the energy balance described in Section 3, which is expressed in terms of power contributions, in the present section the energy balance is written in terms of energy components for the ease of analysis. Thus, the following energy budget is used:

$$\boxed{\mathcal{E}_k + \mathcal{E}_p + \mathcal{E}_c = \mathcal{W}_\mu + \mathcal{W}_{Rie} + \mathcal{W}_{\delta u}} \tag{43}$$

where

$$\mathcal{W}_\mu = \int_0^t \mathcal{P}_\mu(\tau)\, d\tau \quad ; \quad \mathcal{W}_{Rie} = \int_0^t \mathcal{P}_{Rie}(\tau)\, d\tau \quad ; \quad \mathcal{W}_{\delta u} = \int_0^t \left[\mathcal{P}_{\delta u}(\tau) + \mathcal{P}_{\delta u}^f(\tau) \right] d\tau \quad . \tag{44}$$

The kinetic, compressible and (when applicable) potential energy, namely $\mathcal{E}_k$, $\mathcal{E}_c$ and $\mathcal{E}_p$, are computed through Eqs. (27), (28) and (39) respectively, using the state of the fluid at a certain instant, while all the remaining quantities are integrated in time. This allows for a numerical check on the accuracy of the time integration. According to Eq. (43), we require that the variations of the term $|\mathcal{E}_k + \mathcal{E}_p + \mathcal{E}_c - \mathcal{W}_\mu - \mathcal{W}_{Rie} - \mathcal{W}_{\delta u}|$ are negligible in comparison to its single components.

4.1. 2D Taylor–Green vortices

The first test case under investigation is the 2D Taylor–Green vortex flow [57], for which the use of PST is of fundamental importance (see *e.g.* [2,3]). In particular, it has been shown that for quasi-Lagrangian formulations the PST can be crucial to avoid a drift of the average pressure field (see *e.g.* [6,7]). Therefore, it is important to study the role of the different energy components and, specifically, those due to the PST terms.

The analytical solution in terms of velocity and pressure is given by:

$$u_x = U \sin\left(2\pi x/L\right) \cos\left(2\pi y/L\right) e^{\left(-8\pi^2/Re\right)tU/L} \tag{45}$$

$$u_y = -U \cos\left(2\pi x/L\right) \sin\left(2\pi y/L\right) e^{\left(-8\pi^2/Re\right)tU/L} \tag{46}$$

$$p = \frac{\rho_0 U^2}{2} \frac{1}{2} \left[\cos\left(4\pi x/L\right) + \cos\left(4\pi y/L\right)\right] e^{\left(-16\pi^2/Re\right)tU/L} \tag{47}$$
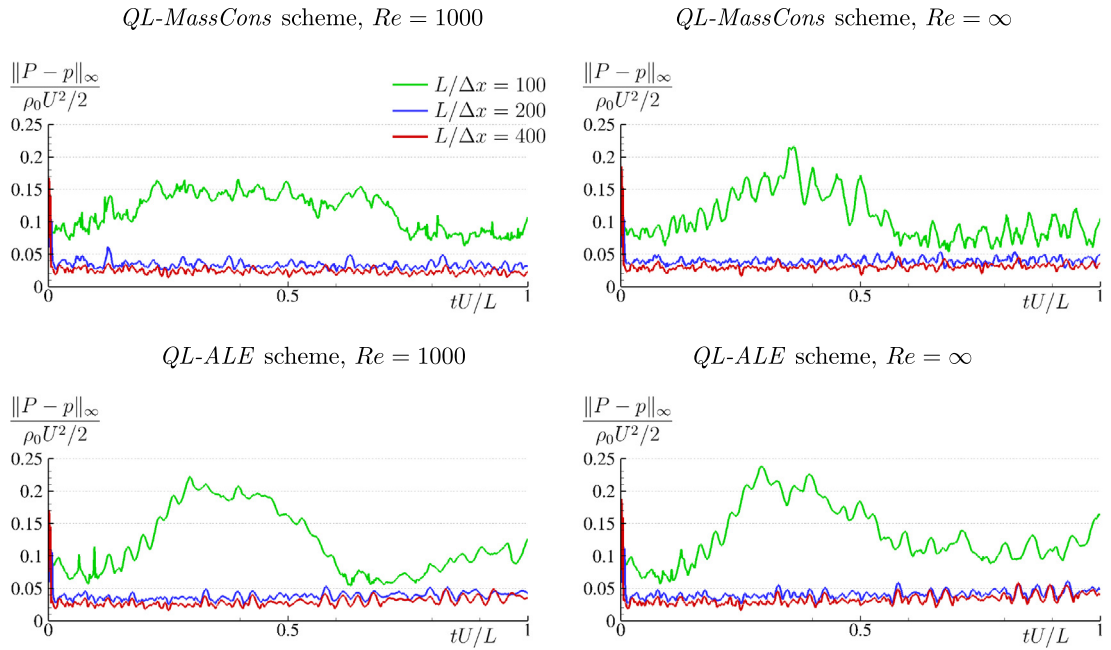
Fig. 2. 2D Taylor–Green vortices. Time evolution of the error on the pressure with respect to the analytical pressure p (defined in Eq. (47)) measured using the L^∞ norm, for three spatial resolutions. Left: $Re = 1000$. Right: $Re = \infty$. Top: *QL-MassCons* scheme. Bottom: *QL-ALE* scheme.

in a periodic domain of size $[0, L] \times [0, L]$. The analytical kinetic energy is $\mathcal{E}_k(tU/L) = \mathcal{E}_k^0 e^{(-16\pi^2/Re)tU/L}$, with $\mathcal{E}_k^0$ the initial kinetic energy. In order to study the influence of viscous effects on the energy balance the problem is solved for an inviscid fluid, *i.e.* $Re = \infty$, and for a viscous fluid at $Re = 1000$. The reference scales are the length L, the velocity U, the time L/U, the pressure $\rho_0 U^2/2$, and the initial kinetic energy $\mathcal{E}_k^0$. The nominal sound speed is taken as $c_0 = 10U$. Particle positions are initialized by using the packing algorithm described in [58] with a slight modification. Specifically, the particle motion is computed through Eq. (24) instead of $\nabla \Gamma_i$ as originally proposed in [58].

In Fig. 2 the time evolution of the error on the pressure field in the L^∞ norm is shown for the two schemes at $Re = 1000$ and $Re = \infty$. For each case three different resolutions are adopted, namely $L/\Delta x = 100, 200, 400$. In all the simulations, the numerical solution converges towards the analytical solution when refining the spatial resolution. The error is less than about 5% with respect to the reference pressure for spatial resolutions $L/\Delta x \geq 200$.

In fact, this error is concentrated on a few particles located in flow bifurcation regions (i.e. at the centre of the fluid domain). In any case satisfactory results are obtained, as displayed in Fig. 3 where the pressure field obtained with the *QL-MassCons* scheme at $tU/L = 1$ with $L/\Delta x = 100$ is represented for $Re = 1000$ (left plot) and $Re = \infty$ (right plot); in each plot, the analytical solution is provided on the right hand side of the vertical black dashed-line.

As observed in Fig. 4 the kinetic energy rapidly tends to the analytical one. For $L/\Delta x \geq 200$, the relative error with respect to the analytical kinetic energy is smaller than 0.5% at $tU/L = 1$ for both $Re = 1000$ and $Re = \infty$; the kinetic energy obtained with the *QL-ALE* scheme is not represented here since the results are very similar (see for example Fig. 6). The compressible energy $\mathcal{E}_c$ is negligible in this case, since the maximum amplitude of the oscillations of $\mathcal{E}_c$ is smaller than $0.02\% \mathcal{E}_k^0$.

With respect to the literature, these results are very similar in terms of error on the kinetic energy to those obtained in [3,22] with the Vila's scheme.

The energy balance performed in Section 3 allows us to investigate which are the predominant terms involved in the numerical dissipation process. The results are reported in Fig. 5.
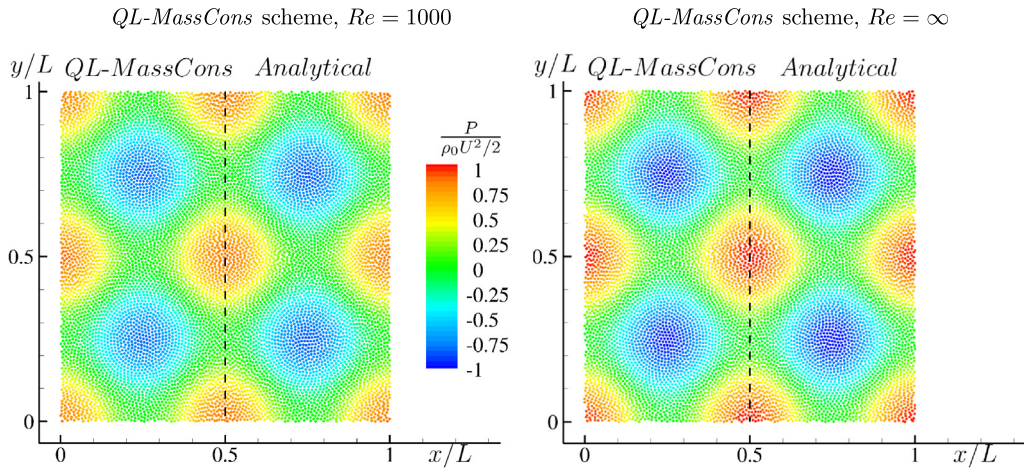
Fig. 3. 2D Taylor–Green vortices. Pressure fields obtained at $tU/L = 1$ with the *QL-MassCons* scheme for $L/\Delta x = 100$ at $Re = 1000$ (left plot) and $Re = \infty$ (right plot). The analytical solution is provided on the right part of each plot for qualitative comparison purposes.
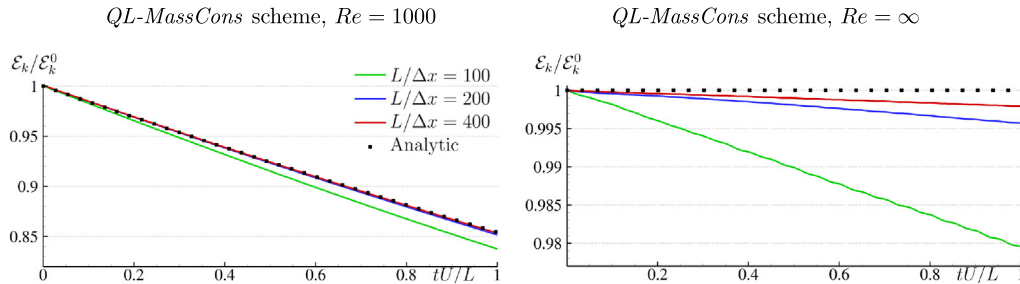

Fig. 4. 2D Taylor–Green vortices. Time evolution of the kinetic energy obtained with the *QL-MassCons* scheme with three spatial resolutions and comparison with the analytical solution $e^{(-16\pi^2/Re)tU/L}$. Left: $Re = 1000$. Right: $Re = \infty$.

At $Re = 1000$, the dissipation is substantially driven by the viscous term $\mathcal{W}_\mu$, as expected. Both the Riemann and PST energy terms exhibit a purely diffusive contribution and account for about 1% and 0.1%, respectively, of the total dissipation for the coarsest resolution.

About the PST energy term $\mathcal{W}_{\delta u}$, most of its contribution is due to $\mathcal{P}^{cont}_{\delta u}$. This explains the diffusive behaviour of $\mathcal{W}_{\delta u}$, as the PST acts mainly in the bifurcation zones where the pressure is positive (see the discussion in Section 3). In Fig. 6 the convergence analysis of the different energy terms is reported. For the Riemann term $\mathcal{W}_{Rie}$, a 3th-order convergence is observed. By contrast, $\mathcal{W}_{\delta u}$ remains almost constant for the three spatial resolutions. Again, this behaviour is due to the term $\mathcal{P}^{cont}_{\delta u}$ and is in accordance with the convergence properties described in Section 3. Nevertheless, the numerical dissipation induced by the PST is two order of magnitude smaller than the viscous one. Therefore, one can conclude that the numerical dissipation introduced by the PST is relatively small with respect to its benefits. This is in agreement with the findings in [3] where it was shown that purely Lagrangian schemes are more dissipative than quasi-Lagrangian ones.

At $Re = \infty$, the Riemann and PST energy components behave similarly as at $Re = 1000$ in terms of consistency, amount of energy dissipated and diffusive aspect. Remarkably, for each spatial resolution a similar percentage of energy is dissipated for $Re = 1000$ and $Re = \infty$, implying that the energy dissipation due to Riemann and PST terms in this test case seems independent of the fluid viscosity. More in general, the *QL-ALE* scheme behaves similarly to the *QL-MassCons*, because the variation of the particles' masses is rather small. This is shown in Fig. 6, where the energy dissipated by each component (viscosity, Riemann and PST) at $tU/L = 1$ for the two schemes at $Re = 1000$ are reported as a function of the spatial resolution. Similar results are obtained also at $Re = \infty$.
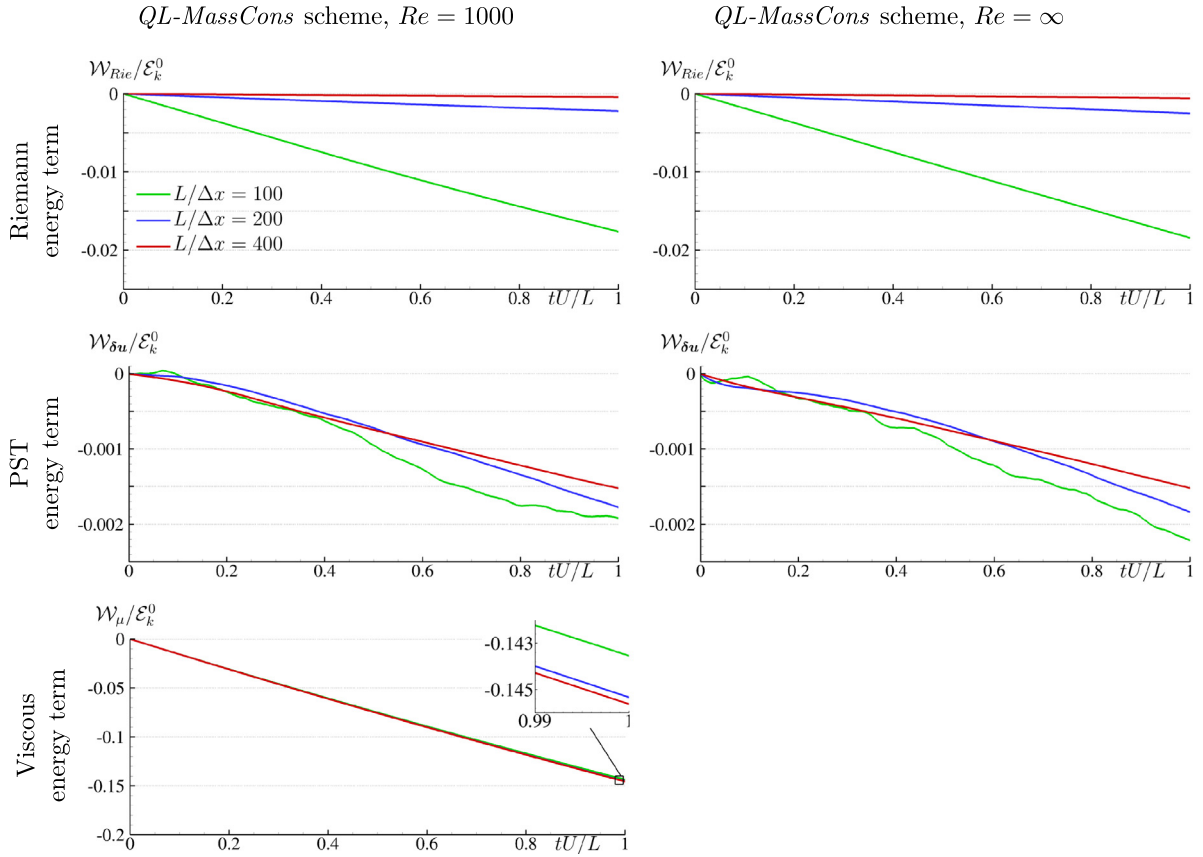
Fig. 5. 2D Taylor–Green vortices. Time evolution of Riemann and PST energy terms (respectively from top to bottom) obtained with the *QL-MassCons* scheme with three spatial resolutions. Left: $Re = 1000$. Right: $Re = \infty$. For $Re = 1000$ the viscous energy term is also plotted.
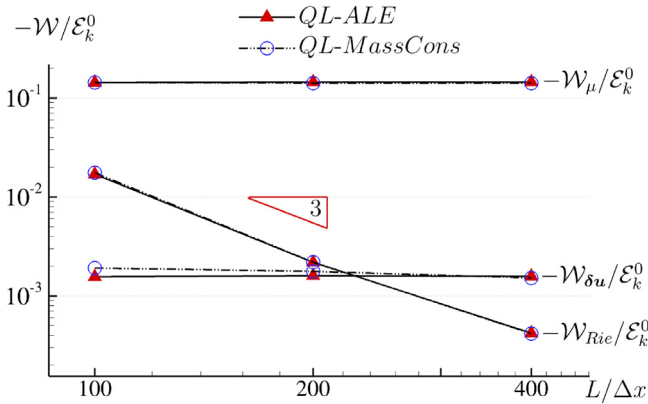

Fig. 6. 2D Taylor–Green vortices. Energy dissipated at $tU/L = 1$ by each component with the *QL-MassCons* and *QL-ALE* schemes at $Re = 1000$, as function of the spatial resolution.

4.1.1. Influence of background pressure on the energy terms

In Section 3 it is shown that the term $\mathcal{P}_{\delta u}^{cont}$ is not invariant by change of the ambient pressure. To verify this, the simulations in Section 4.1 are rerun by adding two different values of the background pressure, namely $P_b = \frac{1}{4}\rho_0 U^2$
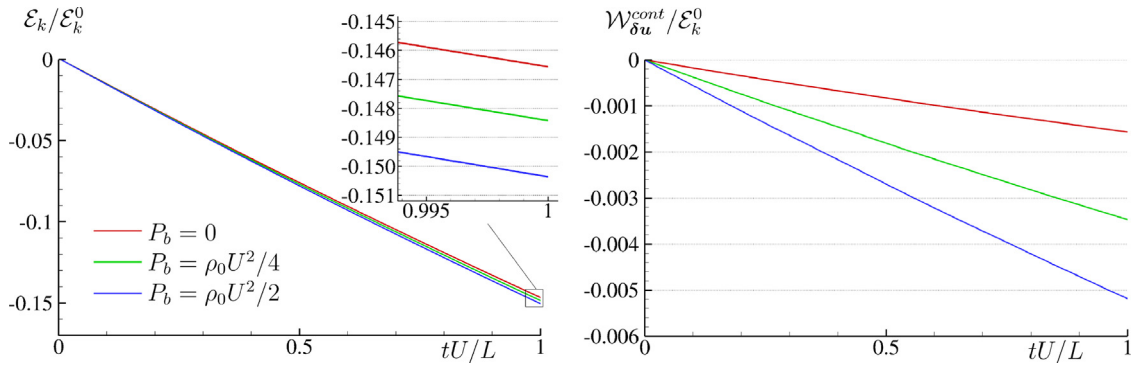
Fig. 7. 2D Taylor–Green vortices. Time evolution of the kinetic energy $\mathcal{E}_k$ (left plot) and the energy term due to the PST within the continuity equation $\mathcal{W}_{\delta u}^{cont} = \int_0^t \mathcal{P}_{\delta u}^{cont} d\tau$ (right plot) obtained with the *QL-MassCons* scheme at $Re = 1000$ with $L/\Delta x = 400$, for three different values of the background pressure namely $P_b = 0$, $P_b = \frac{1}{4}\rho_0 U^2$ and $P_b = \frac{1}{2}\rho_0 U^2$.

and $P_b = \frac{1}{2}\rho_0 U^2$. In the latter case, the pressure is positive overall the fluid domain. In Fig. 7, the kinetic energy $\mathcal{E}_k$ and the energy term $\mathcal{W}_{\delta u}^{cont} = \int_0^t \mathcal{P}_{\delta u}^{cont} d\tau$ are shown for the three different values of P_b at $Re = 1000$ and $L/\Delta x = 400$. The final value of $\mathcal{E}_k$ exhibits a small variation depending on the value of P_b adopted (see the inset in the left plot). This essentially comes from the difference observed on $\mathcal{W}_{\delta u}^{cont}$ (see right plot): as P_b increases, a proportional increase of $\mathcal{W}_{\delta u}^{cont}$ is observed. This confirms the behaviour predicted theoretically in Section 2.4. In any case, the difference observed on $\mathcal{E}_k$ between $P_b = 0$ and $P_b = \frac{1}{2}\rho_0 U^2$ is rather small and represents less than 0.5% at $tU/L = 1$. The results shown here refer to the *QL-MassCons* scheme, but similar outputs are observed for the *QL-ALE* scheme.

4.2. 2D inviscid stretching drop under central conservative forces

The second test case under investigation was developed in [59] and is proposed as Benchmark #1 among the SPHERIC Benchmark Cases.[1] It consists in a periodic oscillating drop of an inviscid fluid under a central conservative force $\boldsymbol{f}_i = -\Omega^2 \boldsymbol{x}_i$ where Ω is a reference frequency parameter. Since the mechanical energy must be conserved, this problem constitutes a test case for studying the different energy components when a free-surface and a conservative volume force are involved. Furthermore, it is interesting since it is analogous to the non-linear oscillation of gravity waves [59].

As shown in [59], the analytical solution for an incompressible fluid is:

$$u_x = \sigma x \tag{48}$$

$$u_y = -\sigma y \tag{49}$$

$$p = \rho_0 \left(\sigma^2 + \Omega^2\right) \left(\frac{b^2 a^2}{b^2 + a^2}\right) \left(1 - \frac{x^2}{a^2} - \frac{y^2}{b^2}\right) \tag{50}$$

where a and b are, respectively, the semi-major and semi-minor axes of the ellipse and σ has dimension of a frequency. These obey to the following system of ordinary differential equations:

$$\begin{cases} \dfrac{da}{dt} = \sigma a \\[2mm] \dfrac{db}{dt} = -\sigma b \\[2mm] \dfrac{d\sigma}{dt} = \left(\Omega^2 + \sigma^2\right)\left(\dfrac{b^2 - a^2}{b^2 + a^2}\right) \end{cases} . \tag{51}$$

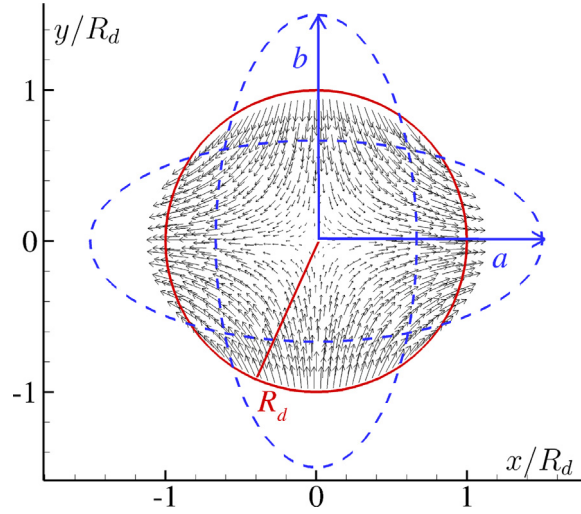[1] www.spheric-sph.org/validation-tests

Fig. 8. 2D oscillating stretching drop. A sketch of the initial configuration when $a = b = R_d$ along with the initial velocity vectors (represented in black). The patch evolves periodically in successive elliptical forms of semi-axes a and b (sketched in blue dashed line). (For interpretation of the references to color in this figure legend, the reader is referred to the web version of this article.)

Since the fluid is assumed as incompressible, the total volume of the fluid is theoretically conserved, implying that a and b are linked by the relation $ab = R_d^2$ with R_d the radius of the circle when $a = b$. The kinetic and potential energies can be computed analytically as follows:

$$\mathcal{E}_k = \int \rho \frac{\|\boldsymbol{u}\|^2}{2} dV = \int \rho \sigma^2 \frac{\|\boldsymbol{x}\|^2}{2} dV = \pi R_d^2 \rho_0 \sigma^2 (a^2 + b^2)/8 \,,$$

$$\mathcal{E}_p = \int \rho \Omega^2 \frac{\|\boldsymbol{x}\|^2}{2} dV = \pi R_d^2 \rho_0 \Omega^2 (a^2 + b^2)/8 \tag{52}$$

The mechanical energy $\mathcal{E}_m = \mathcal{E}_k + \mathcal{E}_p$ is theoretically conserved with $\mathcal{E}_m^0 = \pi R_d^2 \rho_0 (\Omega^2 + \sigma_0^2) R_d^2/4$ where σ_0 is the value of σ when $a = b$. The analytical solution is obtained by resolving numerically (51), prior to the simulations. The reference scales are the length R_d, the oscillation time T, the reference pressure $P_{ref} = \rho_0 R_d^2 \left(\sigma_0^2 + \Omega^2\right)/2$ and the energy $\mathcal{E}_m^0$. The dynamics of the flow is governed by the ratio σ_0/Ω.

4.2.1. Validation and study of the energy balance for $\sigma_0/\Omega = 1$

In this work, the initial configuration is a circle of centre $(0, 0)$ such that $a = b = R_d$ (see Fig. 8). The particle positions are initialized using the packing algorithm described in [58]. The initial velocity and pressure are set by using $\sigma = \sigma_0$ in Eqs. (48)–(50) and $a = b = R_d$ in Eq. (50). The speed of sound c_0 is chosen such that Eq. (2) is satisfied. Specifically, the expected maximum velocity and pressure variation are determined using the semi-analytical resolution of (48)–(51), prior to the simulations. The simulations are performed for 10 periods of oscillation of the stretching drop and for three spatial resolutions, namely $R_d/\Delta x = 50, 100, 200$.

In Fig. 9 the time evolution of the pressure at two different spatial locations is plotted and compared to the analytical solution. A very good agreement is found with both the *QL-MassCons* and *QL-ALE* schemes, even for the coarsest spatial resolution.

The results obtained with the *QL-MassCons* and *QL-ALE* schemes in terms of time evolution of the semi-major axes a are reported in Fig. 10. After 10 oscillations the relative error on a is smaller than 2.5% with respect to the analytical solution whatever the spatial resolution used. Numerical convergence is observed for both schemes, with an error of about 1% for the finest resolution.

In Fig. 11 the pressure field obtained during the last oscillation is represented for $R_d/\Delta x = 50$ at two specific time instants, namely when the drop is circular (left plot) and for the maximum horizontal elongation (right plot). The analytical free-surface shape is represented with dashed line for comparison purposes. In addition, on each
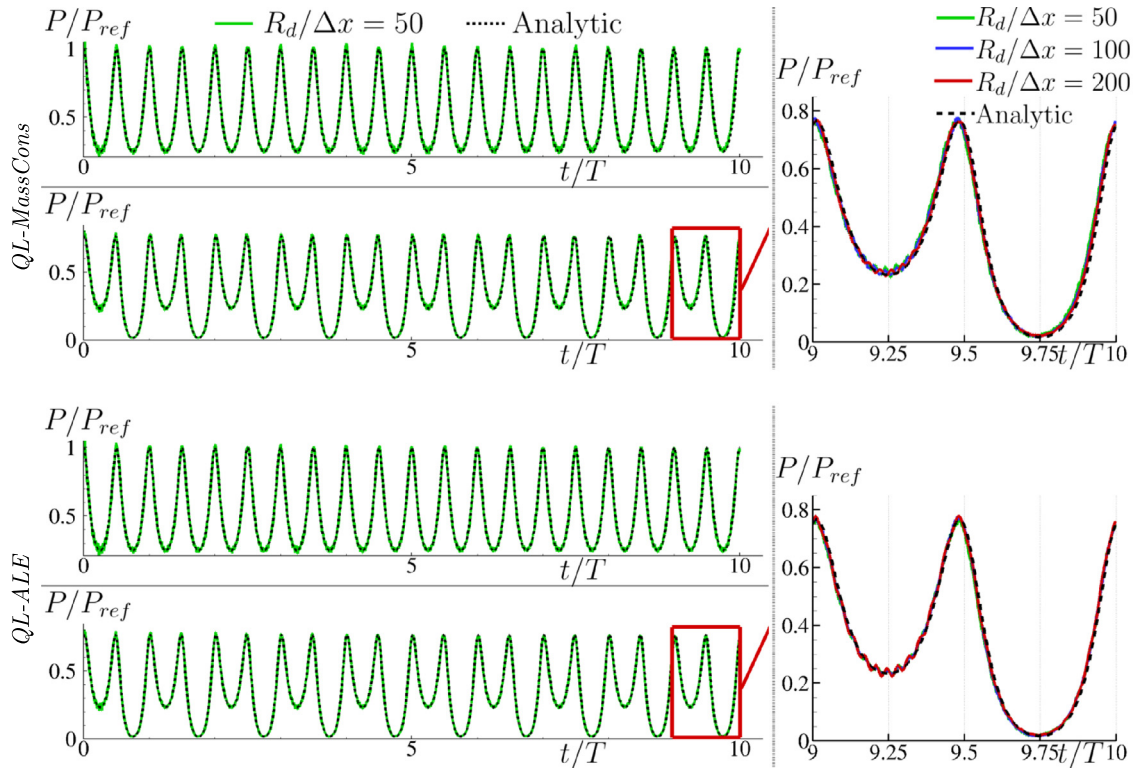
Fig. 9. 2D oscillating stretching drop with $\sigma_0/\Omega = 1$. Time evolution of the pressure obtained with the *QL-MassCons* scheme (top) and *QL-ALE* scheme (bottom). For each scheme, on the left the pressure measured at the centre of fluid domain $(x/R_d, y/R_d) = (0,0)$ and at $(x/R_d, y/R_d) = (0.5;0)$ for $R_d/\Delta x = 50$ is compared to the analytical solution. On the right, a zoom of the last pressure oscillation at $(x/R_d, y/R_d) = (0.5, 0)$ for three spatial resolutions is reported for each scheme. In all the cases $P_{ref} = \rho_0 R_d^2 \left(\sigma_0^2 + \Omega^2\right)/2$.

plot, the analytical pressure field is shown in the right-hand side of the vertical dashed line, *i.e.* where $x/R_d > 0$. A very good agreement is also obtained in this comparison as only slight discrepancies are observed consequently to the energy dissipated after ten periods.

Regarding the total energy (top part of Fig. 12), a similar behaviour between the *QL-MassCons* and *QL-ALE* schemes is observed in terms of both convergence rate and absolute errors. In particular, the numerical dissipation with respect to the analytical solution $\mathcal{E}_m^0$ is smaller than 2.5% after 10 oscillations for $R_d/\Delta x = 50$. This value is slightly smaller with respect to the results presented in [16]. Furthermore, we observe a periodic pattern within the signal of the total energy time history. This is a consequence of the fact that the largest part of the numerical dissipation occurs around the instant when the drop is circular, *i.e.* around the instants of maximum pressure, pressure gradients, velocity and velocity gradients.

The energy terms involved in the dissipation process are shown in the middle and bottom parts of Fig. 12. Similarly to the previous test case, a purely diffusive behaviour is observed for the Riemann term $\mathcal{W}_{Rie}$. The PST term $\mathcal{W}_{\delta u}$ presents also a diffusive behaviour, except at the beginning of the simulation with the *QL-MassCons* scheme for $R_d/\Delta x = 50$. The periodic pattern observed on the total energy is, in fact, due to the combination of the Riemann and PST terms, whose maximum dissipation occurs, in both cases, around the instants where the drop is circular. Since the maximum pressure and velocity gradients take place at such instants, the Riemann term $\mathcal{W}_{Rie}$ presents its maximum dissipation (see Eqs. (31) and (32)). Regarding $\mathcal{W}_{\delta u}$, the PST acts more in zone of high velocity gradient because the magnitude of δu_i is driven by the maximum relative velocity. In addition, this corresponds to instants of maximum pressure and, thus, further increases the contribution of $\mathcal{W}_{\delta u}$ (see Eq. (42)).

About the consistency of the Riemann term, it converges towards 0 when the spatial resolution increases, with a saturation observed on the convergence order (see the left panel of Fig. 13). It is worth noting that $\mathcal{W}_{Rie}$
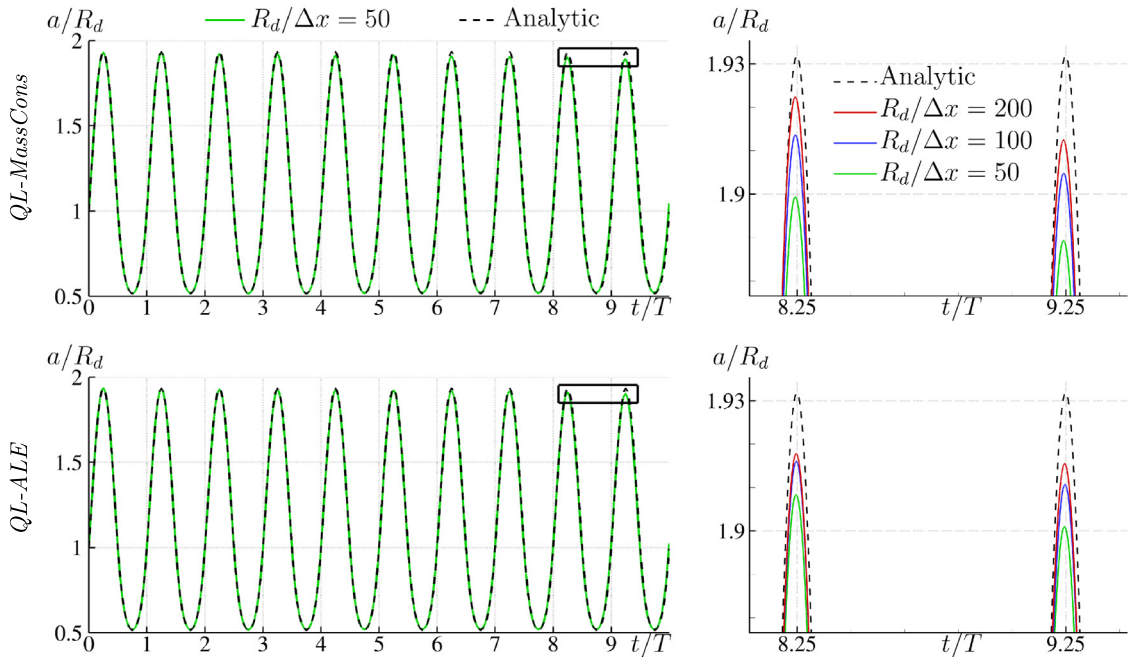
Fig. 10. 2D oscillating stretching drop with $\sigma_0/\Omega = 1$. Time evolution of the major semi-axes a and comparison to the analytical solution. Left: comparison between $R_d/\Delta x = 50$ and the analytical solution. Right: zoom around the last oscillations for three spatial resolutions. Top: *QL-MassCons* scheme. Bottom: *QL-ALE* scheme.
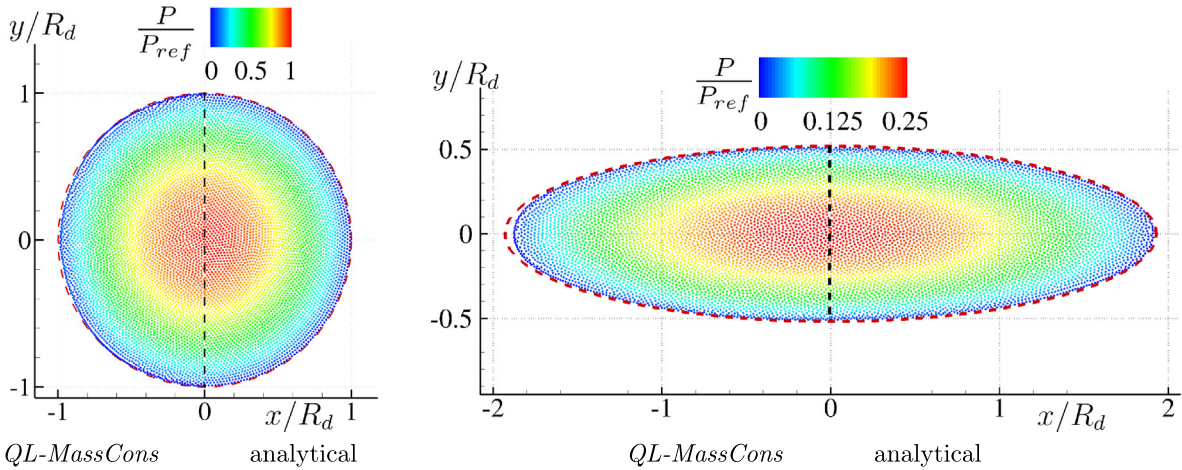

Fig. 11. 2D oscillating stretching drop with $\sigma_0/\Omega = 1$. Pressure field at $t/T \approx 10$ (left plot) and $t/T \approx 9.25$ (right plot) with $R_d/\Delta x = 50$. On each plot, the solution obtained with the *QL-MassCons* scheme is represented on the left part of the black-dashed line whereas the analytical solution is plotted on the right part of the black-dashed line. The analytical free-surface is also plotted in red dashed line. In all the cases $P_{ref} = \rho_0 R_d^2 \left(\sigma_0^2 + \Omega^2\right)/2$. (For interpretation of the references to color in this figure legend, the reader is referred to the web version of this article.)

behaves slightly differently between the *QL-MassCons* and *QL-ALE* schemes, while more pronounced differences are observed for $\mathcal{W}_{\delta u}$ (see the right panel of Fig. 13). In particular, the PST term converges towards the value $-0.01\mathcal{E}_m^0$ at $t/T = 10$ for the *QL-MassCons* scheme, whereas in the *QL-ALE* scheme $\mathcal{W}_{\delta u}$ remains close to this value for all the resolutions (bottom panels of Fig. 12). In fact, the value $-0.01\mathcal{E}_m^0$ is mainly given by the term $\mathcal{P}_{\delta u}^{cont}$ which is little influenced by the spatial resolution, as predicted by the theory (see Section 3). The variations
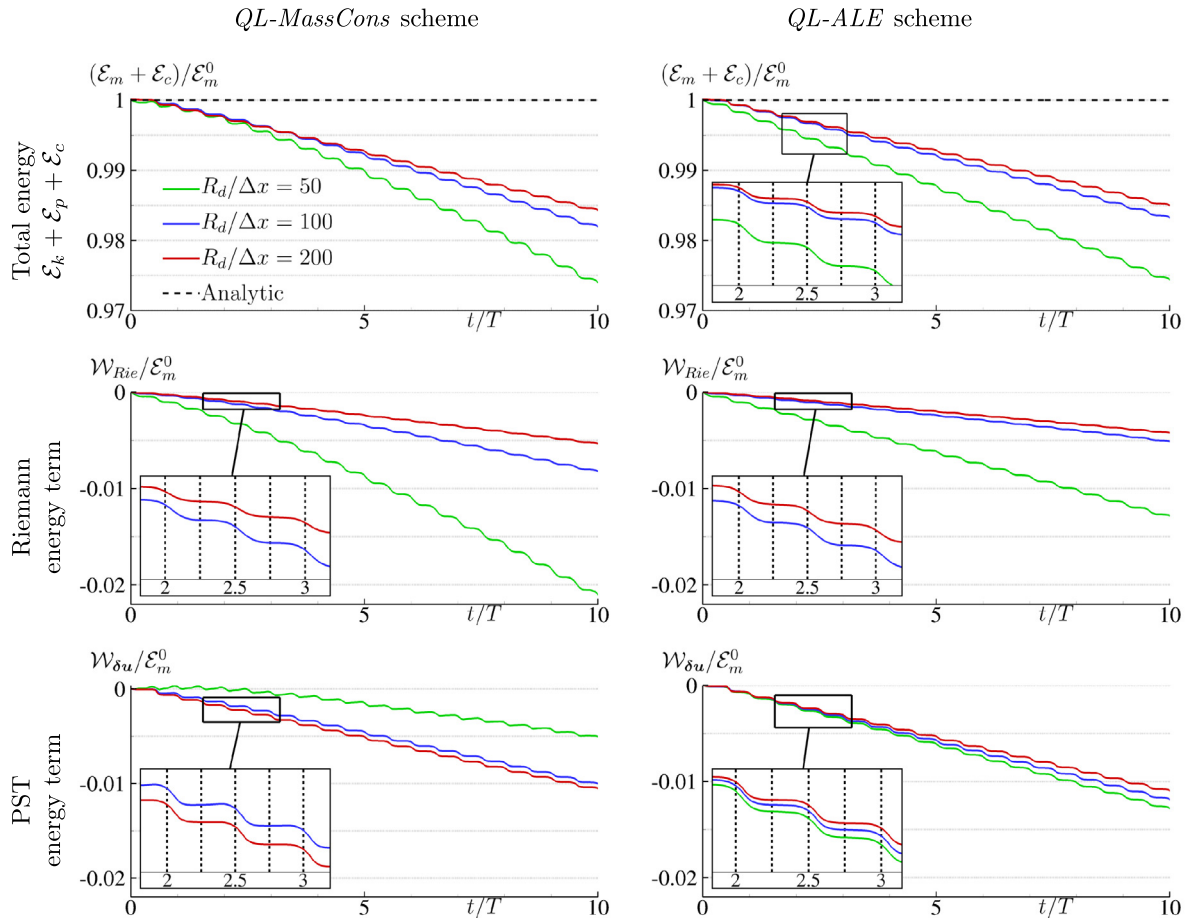
Fig. 12. 2D oscillating stretching drop with $\sigma_0/\Omega = 1$. Time evolution of the total, Riemann, and PST energy terms (from top to bottom) obtained with the *QL-MassCons* scheme (left) and *QL-ALE* scheme (right) for three spatial resolutions. The total energy is compared to the analytical solution.

around this value are due to $\mathcal{P}_{\delta u}^{mom}$ and $\mathcal{P}_{\delta u}^{f}$, which behave differently between the *QL-MassCons* and the *QL-ALE* schemes (even though they both converge towards zero). Remarkably, even if $\mathcal{W}_{\delta u}$ and $\mathcal{W}_{Rie}$ exhibit different values between the *QL-MassCons* and *QL-ALE* schemes (especially for the coarse resolution), we can observe that (i) their sum is approximately equal between the two schemes (similarly to the total energy), and (ii) these differences tend to vanish when the spatial resolution increases. In fact, the differences observed between the two schemes can be ascribed to non-negligible local mass variations occurring in the *QL-ALE* scheme due to the action of the PST.

4.2.2. Influence of the ratio σ_0/Ω

Similarly to [16], in this section we propose a study of the energy components by varying the ratio σ_0/Ω. In this case the spatial resolution is $R_d/\Delta x = 200$ (like in [16]) and the numerical results are displayed in Fig. 14. Note that the analysis is provided only for the *QL-MassCons* scheme since a similar behaviour is observed using the *QL-ALE* scheme.

Regarding the total energy, we observe that the dissipation increases as the dynamics of the case increases (top left panel in Fig. 14). This is in agreement with the behaviour observed in [16] where a purely Lagrangian formulation was used. Differently from [16], however, we observe that the present formulations allow for better results when high values of the ratio σ_0/Ω are considered. In fact, for stronger dynamics, larger deformations of the fluid domain are observed (see, for example, the top right panel of Fig. 14) and the use of a PST becomes crucial to maintain a uniform particle distribution and a low interpolation error. This behaviour is highlighted in the bottom right panel
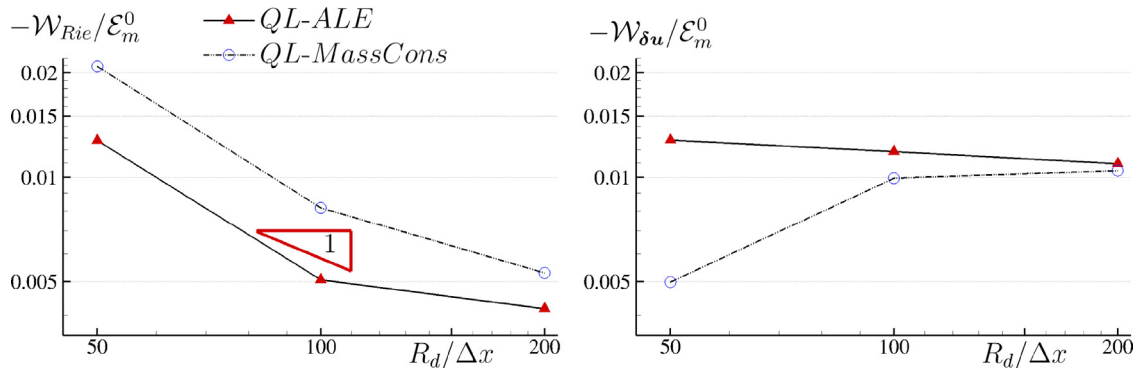
Fig. 13. 2D oscillating stretching drop with $\sigma_0/\Omega = 1$. Energy dissipated at $t/T = 10$ by $\mathcal{W}_{Rie}$ (left) and $\mathcal{W}_{\delta u}$ (right) with the *QL-MassCons* and *QL-ALE* schemes, as a function of the spatial resolution.
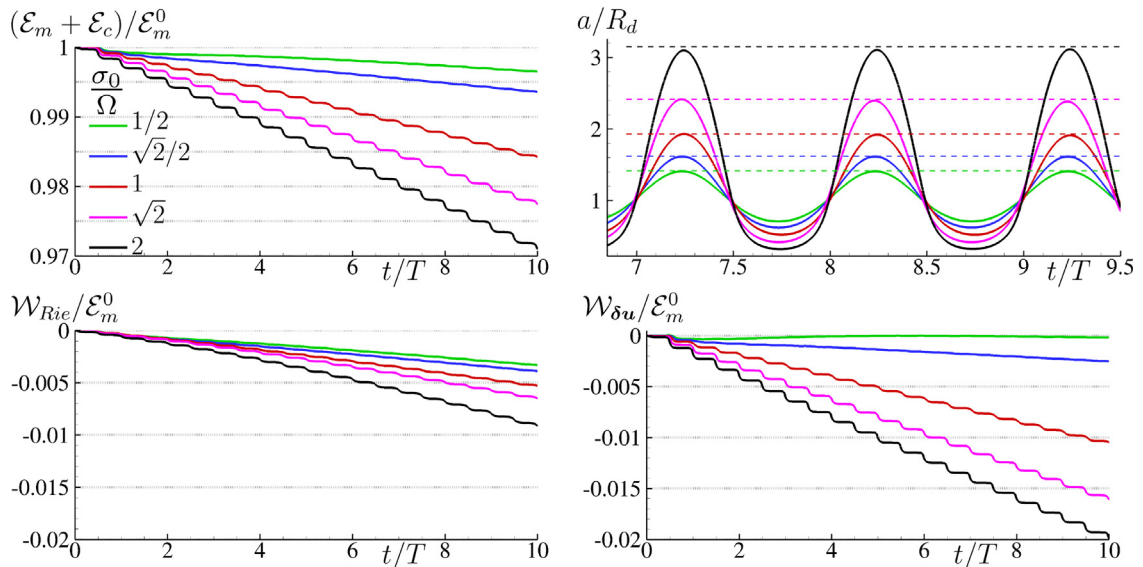

Fig. 14. 2D oscillating stretching drop with $R_d/\Delta x = 200$. Time evolution of the total energy (top left), of the semi-axes a (top right), of the Riemann energy term (bottom left), and PST energy term (bottom right) obtained with the *QL-MassCons* scheme for different values of σ_0/Ω. The maximum analytical elongation is plotted in dashed lines in the top right part for comparison purposes.

of Fig. 14 where the energy dissipated by the PST, namely $\mathcal{W}_{\delta u}$, increases as σ_0/Ω increases, whereas it becomes negligible for the lowest value. The periodic pattern on the dissipation process is observed in any case, and the stronger the dynamics, the larger the dissipation around the instant when the fluid is close to its circular form. For low dynamics, the global dissipation is driven by $\mathcal{W}_{Rie}$, whereas $\mathcal{W}_{\delta u}$ becomes predominant when increasing the dynamics. In any case, satisfactory results are obtained since only 3% of the total energy is dissipated after 10 oscillations for the strongest dynamics.

4.3. Impact of two inviscid fluid patches in 2D

The third test case under investigation is the normal impact of two identical rectangular inviscid fluid patches of size $[2L, L]$. The two patches collide with velocities U and $-U$ respectively (see initial configuration in the first plot of Fig. 16). The reference length, time and pressure are L, L/U and $\rho_0 c_0 U$ respectively, where the notation $U = \|U\|$ is used hereinafter. The reference energy is the initial kinetic energy, namely $\mathcal{E}_k^0 = 2\rho_0 L^2 U^2$. This problem was firstly formulated by [60] for an incompressible fluid; in that work the analytical estimation of the
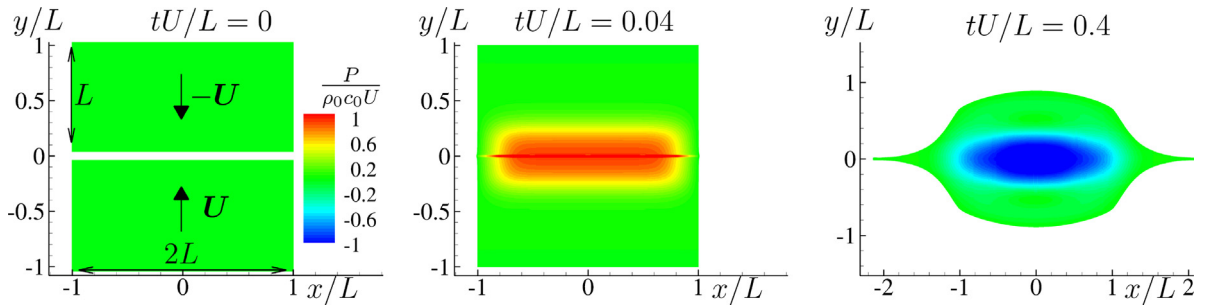
Fig. 15. Impact of two identical inviscid fluid patches in 2D. Evolution of the pressure field as obtained through the *QL-MassCons* scheme with $L/\Delta x = 200$ for three different time instants.

kinetic energy lost during the collision was provided. More recently [27] provided a numerical solution using a weakly-compressible SPH model.

The particles are initialized on a Cartesian lattice with $P = 0$, $u_x = 0$ and $u_y = \pm U$. The speed of sound is equal to $c_0 = 100U$ as in [27] in order to have maximum density variation of the order of 1%. The test case is initialized using a small gap of length $0.08L$ between the two fluid patches, as displayed in the left plot of Fig. 15, implying that the impact takes place theoretically at $tU/L = 0.04$ (middle plot). After the contact of the two fluid surfaces, an acoustic wave front propagates in the vertical direction from the contact line towards the free surface with intensity of order $\rho_0 c_0 U$. At the same time, a rarefaction wave is reflected by the lateral free surfaces and moves horizontally towards the centre (middle plot of Fig. 15). After that, the two joint fluid patches experience a deformation stage with a horizontal elongation (right plot of Fig. 15). The acoustic waves keep reflecting on the deforming free surface as the fluid patch elongates.

From a global viewpoint, a periodic energy transfer from kinetic to compressible energy (and viceversa) occurs during the multiple reflections of the acoustic waves. Differently from the incompressible case, the total energy $\mathcal{E}_k + \mathcal{E}_c$ is conserved during the impact. The kinetic energy results from a superposition of a constant component associated to the fluid patch elongation (equal to 50% of the initial kinetic energy and standing for the incompressible part of the solution as found by [60]) plus an oscillatory perturbation associated to the generated acoustic waves (see [61]).

This benchmark is of interest since it allows (i) investigating the different energy contributions during impacts; (ii) analysing a problem where the compressible energy is not negligible, differently from the previous test cases; (iii) studying a case where the pressure field is alternatively positive and negative in time. The presence of an initial gap between the fluid patches makes this test case particularly challenging, since the PST can induce an abrupt particle settlement in order to fill the void. In any case, the limitation to the density variation described in Eq. (23) eliminates this issue and allows for simulations that are close to those obtained by using purely Lagrangian schemes (see Fig. 16).

Regarding the kinematics, the results are compared to those obtained in [27] with an incompressible Finite Volume method (LS-FVM): a very good agreement is obtained for both the *QL-MassCons* and *QL-ALE* schemes, as shown in the left plot of Fig. 17. However, a difference is observed between *QL-MassCons* and *QL-ALE* schemes on the particle distribution, as shown in the right part of Fig. 17 where the contour plot of the particle masses is depicted. For the *QL-MassCons* scheme the mass field is trivially constant and an isotropic particles distribution in the impact zone is observed. Conversely, using the *QL-ALE* scheme, strong variations of local masses are observed and this phenomenon also reflects on the particle spatial distribution. More precisely, a mass transfer occurs from the particles located directly on the contact line (*i.e.* $|y|/L < 0.005$) to their neighbour particles. As shown in the left plot of Fig. 17, the pressure field is little affected by this strong variations of masses, meaning that the density is, however, correctly evaluated. This phenomenon was already observed in the SPH literature: in [7] using Riemann terms within the Vila's scheme [9], and in [10] where this issue was mitigated by introducing a diffusive term within the mass equation.

The time evolution of the total energy is plotted in Fig. 18. During the impact stage (*i.e.* up to $tU/L = 0.05$) we observe that the *QL-MassCons* and *QL-ALE* schemes behave similarly to the purely Lagrangian scheme: the
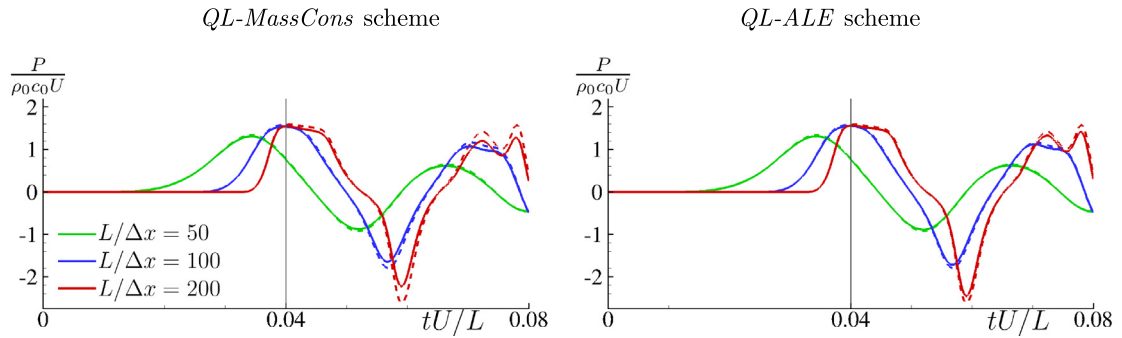
Fig. 16. Impact of two inviscid fluid patches in 2D. Temporal evolution of the pressure at the centre of the domain around the impact stage for three spatial resolutions. Left: *QL-MassCons* scheme (solid lines) compared to Lagrangian simulations (dashed lines). Right: *QL-ALE* scheme (solid lines) compared to Lagrangian simulations (dashed lines). The purely Lagrangian simulations are obtained using $\delta u_i = 0$ within scheme (9) (or (5) since the two schemes (5) and (9) are equivalent without shifting).
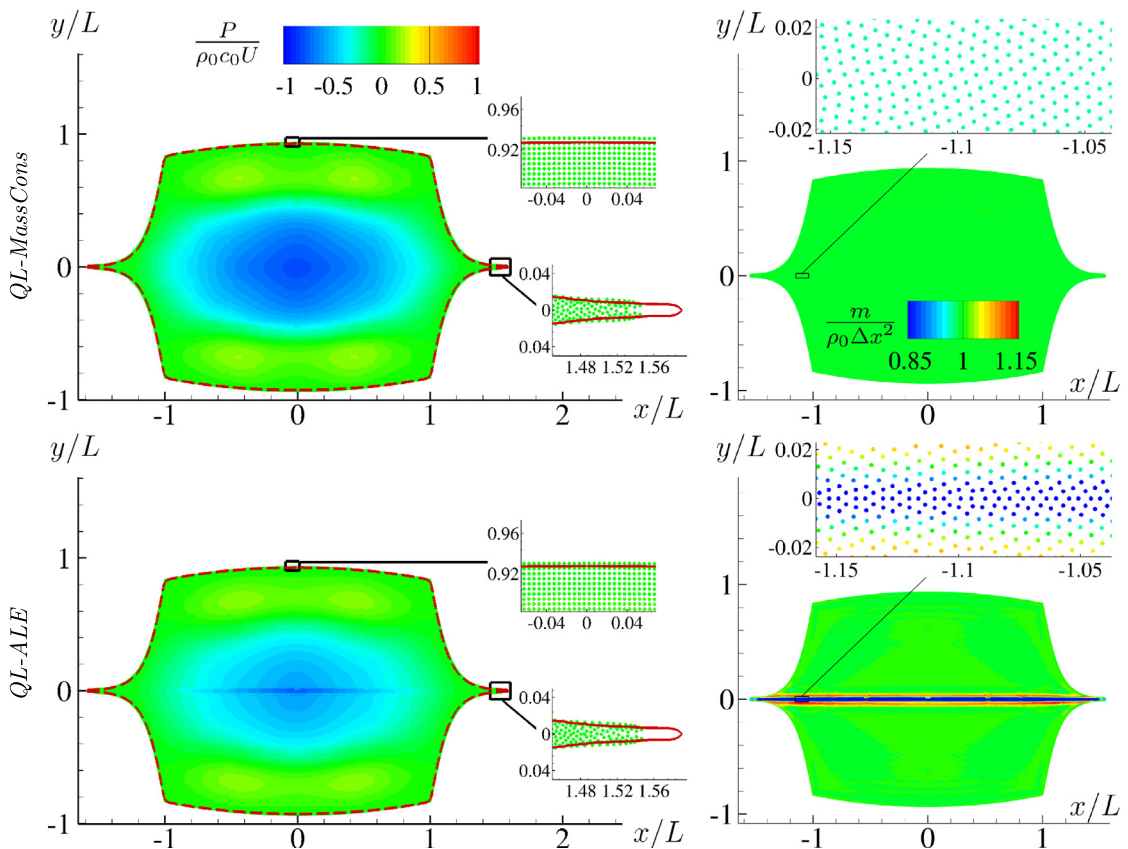

Fig. 17. Impact of two identical inviscid fluid patches in 2D. Left: pressure field obtained at $tU/L = 0.207$ and $L/\Delta x = 200$, and comparison of the free-surface to the one obtained with LS-FVM [27] (dashed line). The LS-FVM time has been re-scaled for comparison purposes. Right: mass field obtained $tU/L = 0.207$ and $L/\Delta x = 200$. Top: *QL-MassCons* scheme. Bottom: *QL-ALE* scheme.

same amount of energy is dissipated, and it decreases as the spatial resolution increases. On the contrary, the quasi-Lagrangian schemes behave differently than the purely Lagrangian scheme, during the elongation stage (*i.e.* for $tU/L > 0.05$). In Lagrangian simulations the energy remained after the impact is progressively dissipated until it reaches about 50% of the initial total energy. This is caused by the disordered particle distribution occurring in
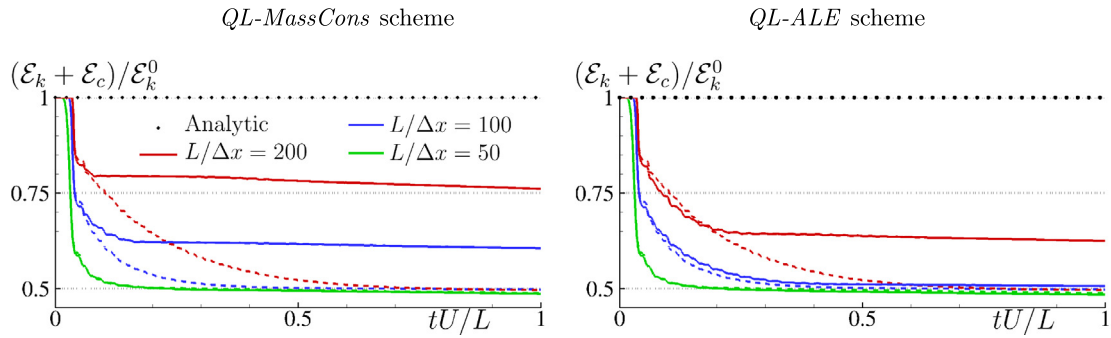
Fig. 18. Impact of two identical inviscid fluid patches in 2D. Temporal evolution of the total energy $\mathcal{E}_k + \mathcal{E}_c$ for three spatial resolutions. Left: *QL-MassCons* scheme (solid lines) compared to Lagrangian simulations (dashed lines). Right: *QL-ALE* scheme (solid lines) compared to Lagrangian simulations (dashed lines).
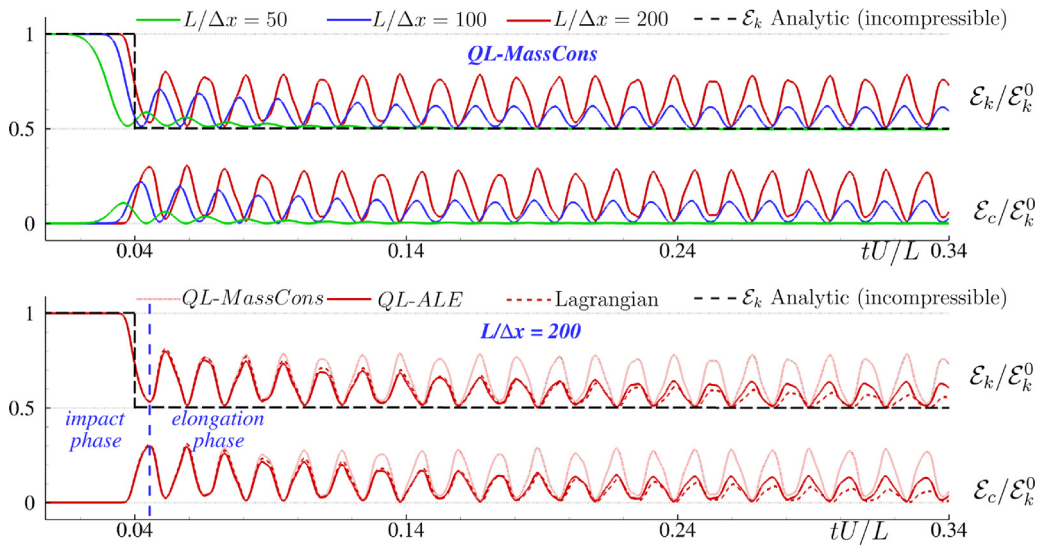

Fig. 19. Impact of two identical inviscid fluid patches in 2D. Temporal evolution of the kinetic and compressible energies. Top: *QL-MassCons* scheme with three spatial resolutions. Bottom: *QL-MassCons*, *QL-ALE* and Lagrangian schemes with $L/\Delta x = 200$.

purely Lagrangian schemes. On the other hand, the quasi-Lagrangian schemes exhibit a different behaviour: with the *QL-MassCons* scheme, thanks to a regular particle distribution (see top-right plot of Fig. 17), the total energy remains almost constant after the impact for all spatial resolutions; with the *QL-ALE* scheme, since the particle distribution is less regular after the impact (see bottom-right plot of Fig. 17), a significant amount of energy is numerically dissipated at the beginning of the elongation stage.

In fact, the differences observed on the evolution of the total energy are associated only to the dissipation of the acoustic component of the solution, while the incompressible component of the kinetic energy is unaffected by both the spatial resolution and the scheme used, as shown in Fig. 19. In any case, as explained in [61], an accurate modelling of the acoustic wave propagation does not substantially affect the patch elongation and, therefore, is not crucial unless the focus of the analysis is on compressible effects. This explains why the free-surface shape obtained with the quasi-Lagrangian schemes matches very well with the results obtained through the incompressible Finite Volume solution (see Fig. 17).

In Fig. 20 the components responsible for the energy dissipation are plotted. The predominant component is the Riemann term $\mathcal{W}_{Rie}$, for which, once again, a purely diffusive behaviour and consistency are observed. In agreement with the results displayed in Fig. 18, the largest part of the dissipation occurs during the impact stage. About the PST term $\mathcal{W}_{\delta u}$, this is about one order of magnitude smaller than the Riemann one. For the coarsest spatial resolutions
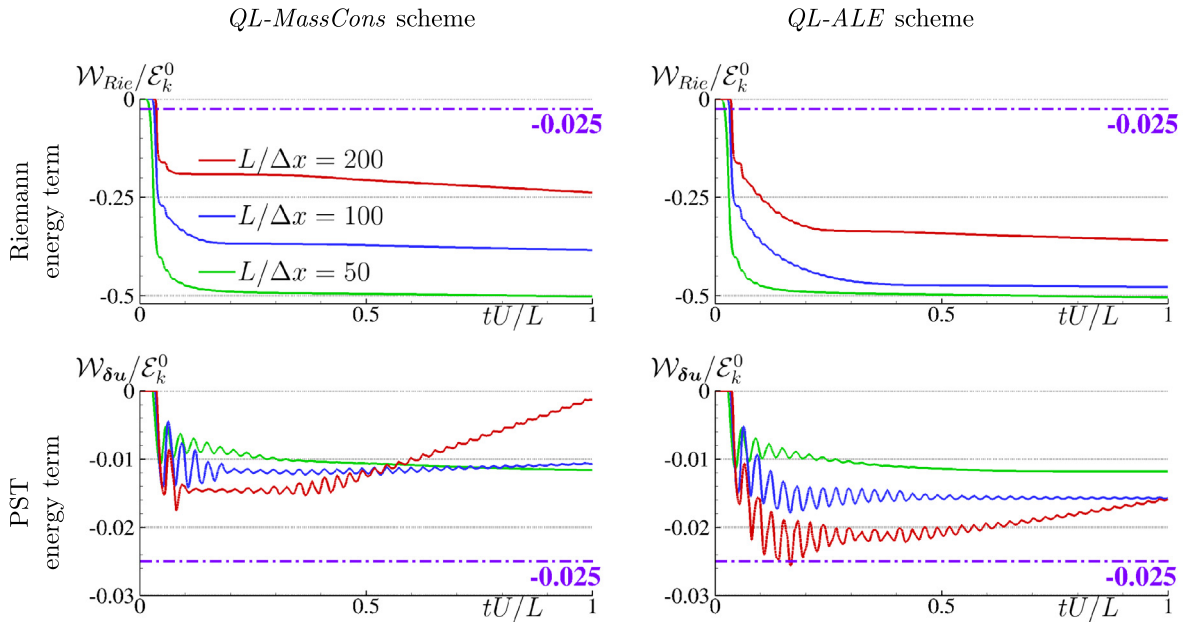
Fig. 20. Impact of two identical inviscid fluid patches in 2D. Time evolution of the Riemann (top) and PST (bottom) energy terms obtained with the *QL-MassCons* scheme (left) and *QL-ALE* scheme (right) for three spatial resolutions. Note that the *y*-scale presents a difference of about one order of magnitude between the Riemann and PST terms. This is highlighted by the purple dot-dashed line representing the same value on all the plots.
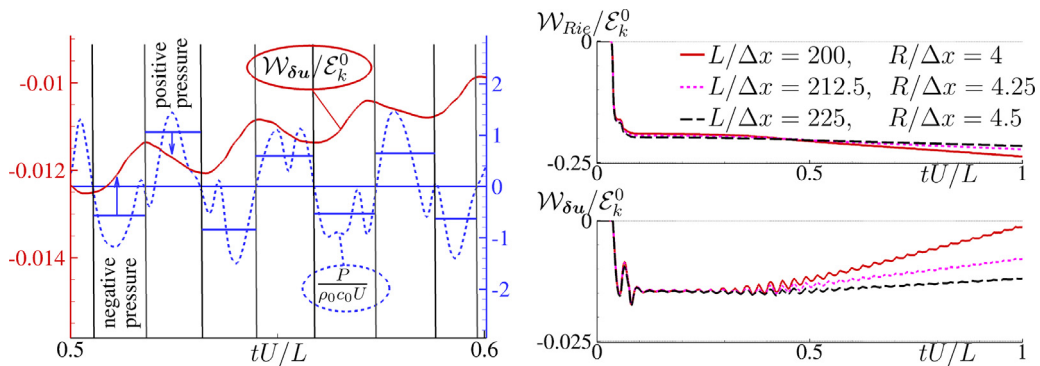

Fig. 21. Impact of two inviscid fluid patches in 2D. Left: time evolution of the pressure at the centre of the fluid domain (blue dashed-line) and of the energy term $\mathcal{W}_{\delta u}$ (red line) highlighting the link existing between pressure sign and contribution of $\mathcal{W}_{\delta u}$; results obtained with the *QL-MassCons* scheme with $L/\Delta x = 200$. Right: temporal evolution of the Riemann (top) and PST (bottom) energy terms as a function of the number of neighbours within the kernel support. (For interpretation of the references to color in this figure legend, the reader is referred to the web version of this article.)

$\mathcal{W}_{\delta u}$ globally exhibits a diffusive behaviour both with the *QL-MassCons* and *QL-ALE* schemes. On the contrary, for the finest resolution (namely, $L/\Delta x = 200$) and for $tU/L > 0.4$, $\mathcal{W}_{\delta u}$ brings energy to the system. Note that, in the same time interval the Riemann term $\mathcal{W}_{Rie}$ increases the amount of dissipated energy counterbalancing the energy brought by $\mathcal{W}_{\delta u}$ so that, globally, both schemes exhibit a diffusive behaviour.

As explained in Section 3, the behaviour of $\mathcal{W}_{\delta u}$ is due to the alternative positive/negative pressure values caused by the generation and propagation of acoustic waves. As shown in the left plot of Fig. 21, $\mathcal{W}_{\delta u}$ represents a dissipation when the pressure is positive, while when the pressure is negative it corresponds to a source of energy. The phenomenon is unbalanced, since the energy brought when the pressure is negative is on average higher than the energy dissipated when the pressure is positive. This may appear odd but is not. Indeed, in regions where the pressure

is negative, the tensile instability is expected to occur and generate voids and disordered particle distributions inside the computational domain. The PST counteracts the tensile instability effect in order to maintain an ordered particle distribution and, therefore, it provides an additional amount of work to the system. The growth in magnitude of the acoustic waves as a consequence of the increase of the spatial resolution motivates the behaviour of $\mathcal{W}_{\delta u}$ for $L/\Delta x = 200$.

This phenomenon can be significantly attenuated by increasing the number of neighbours within the kernel support, *i.e.* reducing the discretization error inherent in the SPH method according to [62]. As shown in the right plot of Fig. 21, the use of a larger number of neighbours within the kernel support implies that (i) the energy brought by $\mathcal{W}_{\delta u}$ is attenuated and (ii) the extra-dissipation observed on the Riemann term $\mathcal{W}_{Rie}$ diminishes, eventually allowing for a better conservation of the total energy during the elongation stage. This applies for both *QL-MassCons* and *QL-ALE* schemes.

5. Conclusion

In the present paper we considered two quasi-Lagrangian SPH schemes which retain the same structure of the models described in [6,10] but include Riemann solvers [13] in place of diffusive terms. The theoretical derivation of the energy balance is provided and the energy contribution of each term appearing in the schemes is well identified. Two major novelties are provided with respect to the literature. On the one hand, the energy contribution provided by Riemann solvers is clearly identified, similarly to what already performed for explicit diffusive terms [16,37]. The energy contribution of the adopted Riemann solver exhibits (i) a purely diffusive behaviour and (ii) consistency, the convergence order depending on the test case under investigation. On the other hand, the energy contribution related to the terms that include the shifting velocity is studied both theoretically and numerically. In particular, some theoretical observations are drawn about the link between the PST terms and the sign of the pressure field. These findings are confirmed by the numerical simulations. Specifically, the PST energy term exhibits a global diffusive behaviour, except when strong negative pressure is observed, and a saturation of the convergence rate when increasing the spatial resolution. In fact, accurate results are found with respect to the reference solutions since, in any case, the PST energy terms give a negligible contribution with respect to the mechanical energy of the system. The differences between the two quasi-Lagrangian formulations are generally small, and mainly occur when large local mass variations are observed.

While the numerical analysis is performed for a specific Riemann solver and a specific PST, the energy balance is written in a manner that can be easily generalized. Specifically, it could be used for comparing different regularization techniques from the standpoint of the energy contribution, for both quasi-Lagrangian and purely Lagrangian formulations. Similarly, different PST strategies can be compared. Furthermore, the theoretical conclusions drawn here constitute a basis for future improvements on the PST itself, specifically in order to obtain the full theoretical and numerical consistency of the PST energy term. Finally, the methodology introduced in the present paper for the derivation of the energy balance can be further extended when other physical effects are considered, like the surface tension, or when other numerical tools are introduced.

Declaration of competing interest

The authors declare the following financial interests/personal relationships which may be considered as potential competing interests: Salvatore Marrone reports financial support was provided by European Union's Horizon 2020.

Data availability

Data will be made available on request.

Acknowledgements

Appendix A. Energy balance for the *QL-ALE* scheme: details of computation

Before proceeding to the derivation of the energy balance for the *QL-ALE* scheme, we briefly recall some basic properties that are used later on to derive the energy contributions. As shown below, many terms of the energy balance are expressed through double summations on the same set of fluid particles (i.e. no solid boundaries are considered). As a consequence, inside these double summations all the anti-symmetric terms with respect to the permutation of the particle indices cancel out exactly, and only the symmetric terms remain. To isolate the symmetric and anti-symmetric contributions, we will use the decompositions $\boldsymbol{u}_i = (\boldsymbol{u}_i - \boldsymbol{u}_j)/2 + (\boldsymbol{u}_i + \boldsymbol{u}_j)/2$, $P_i = (P_i - P_j)/2 + (P_i + P_j)/2$ and the fact that the kernel gradient is anti-symmetric.

The first step to obtain the energy balance is achieved by computing the dot product between the momentum equation in the system (3) and the Lagrangian velocity $\boldsymbol{u}_i$ and, then, summing all over the particles. We find:

$$\sum_i \boldsymbol{u}_i \cdot \frac{d(m_i \boldsymbol{u}_i)}{dt} = -\sum_i V_i \boldsymbol{u}_i \cdot \sum_j (P_i + P_j)\nabla_i W_{ij} V_j + \sum_i m_i \boldsymbol{u}_i \cdot \boldsymbol{f}_i + \sum_i \boldsymbol{u}_i \cdot \Theta_{i,Rie}^{V\rho\boldsymbol{u}}$$
$$+ \sum_i \boldsymbol{u}_i \cdot \boldsymbol{\Pi}_i^{\mu} + \sum_i V_i \boldsymbol{u}_i \cdot \sum_j \left(\rho_i \boldsymbol{u}_i \otimes \delta\boldsymbol{u}_i + \rho_j \boldsymbol{u}_j \otimes \delta\boldsymbol{u}_j\right)\nabla_i W_{ij} V_j$$

where $m_i = \rho_i V_i$ is used. First, we observe that:

$$\boldsymbol{u}_i \cdot \frac{d(m_i \boldsymbol{u}_i)}{dt} = \frac{d}{dt}\left(m_i \frac{\|\boldsymbol{u}_i\|^2}{2}\right) + \frac{\|\boldsymbol{u}_i\|^2}{2}\frac{dm_i}{dt}. \tag{A.1}$$

Substituting the above identity in the equation of the energy balance, we obtain:

$$\frac{d\mathcal{E}_k}{dt} = \overbrace{-\sum_i V_i \boldsymbol{u}_i \cdot \sum_j (P_i + P_j)\nabla_i W_{ij} V_j}^{①} + \overbrace{\sum_i m_i \boldsymbol{u}_i \cdot \boldsymbol{f}_i}^{②} + \overbrace{\sum_i \boldsymbol{u}_i \cdot \Theta_{i,Rie}^{V\rho\boldsymbol{u}}}^{③} + \overbrace{\sum_i \boldsymbol{u}_i \cdot \boldsymbol{\Pi}_i^{\mu}}^{④}$$
$$+ \underbrace{\sum_i V_i \boldsymbol{u}_i \cdot \sum_j \left(\rho_i \boldsymbol{u}_i \otimes \delta\boldsymbol{u}_i + \rho_j \boldsymbol{u}_j \otimes \delta\boldsymbol{u}_j\right)\nabla_i W_{ij} V_j}_{⑤} - \underbrace{\sum_i \frac{\|\boldsymbol{u}_i\|^2}{2}\frac{dm_i}{dt}}_{⑥}$$

where $\mathcal{E}_k$ is the kinetic energy while the term ② is the contribution of the external forces noted $\mathcal{P}_f$. Using the expressions (6) and (13) and the symmetry properties of $\theta_{ij,Rie}^{V\rho\boldsymbol{u}}$ and π_{ij}^{μ}, the terms ③ and ④ are rearranged to give the expressions (30) and (32) respectively. Similarly, the term ⑤ easily reduces to Eq. (34). About the term ⑥, the time derivative of the particle mass is expressed through the third equation in the system (3). Applying the usual symmetry properties, we find the following expression:

$$⑥ = -\sum_i \frac{\|\boldsymbol{u}_i\|^2}{2} V_i \sum (\rho_i \delta\boldsymbol{u}_i + \rho_j \delta\boldsymbol{u}_j)\cdot\nabla_i W_{ij} V_j = -\sum_i \sum_j \frac{\|\boldsymbol{u}_i\|^2 - \|\boldsymbol{u}_j\|^2}{4}(\rho_i \delta\boldsymbol{u}_i + \rho_j \delta\boldsymbol{u}_j)\cdot\nabla_i W_{ij} V_j V_j$$

that corresponds to Eq. (35). Collecting all the above results together, we obtain:

$$\frac{d\mathcal{E}_k}{dt} = \overbrace{-\sum_i V_i \boldsymbol{u}_i \cdot \sum_j (P_i + P_j)\nabla_i W_{ij} V_j}^{①} + \mathcal{P}_f + \mathcal{P}_{Rie}^{mom} + \mathcal{P}_{\mu} + \mathcal{P}_{\delta\boldsymbol{u}}^{mom} + \mathcal{P}_{\delta\boldsymbol{u}}^{m,1} \tag{A.2}$$

The rearrangement of the term ① is more complex and is described below. Using the decomposition of the velocity and pressure fields in their symmetric and anti-symmetric parts and neglecting all the anti-symmetric terms, we find:

$$① = -\sum_i \sum_j V_i V_j (P_j + P_i)\frac{(\boldsymbol{u}_i - \boldsymbol{u}_j)}{2}\cdot\nabla_i W_{ij} - \underbrace{\sum_i \sum_j V_i V_j (P_j + P_i)\frac{(\boldsymbol{u}_i + \boldsymbol{u}_j)}{2}\cdot\nabla_i W_{ij}}_{=0 \text{ (anti-symmetric argument)}}$$
$$= -\sum_i \sum_j V_i V_j \left[2P_i - (P_i - P_j)\right]\frac{(\boldsymbol{u}_i - \boldsymbol{u}_j)}{2}\cdot\nabla_i W_{ij}$$

$$= -\sum_i \sum_j V_i V_j P_i (\boldsymbol{u}_i - \boldsymbol{u}_j) \cdot \boldsymbol{\nabla}_i W_{ij} + \underbrace{\sum_i \sum_j V_i V_j (P_i - P_j) \frac{(\boldsymbol{u}_i - \boldsymbol{u}_j)}{2} \cdot \boldsymbol{\nabla}_i W_{ij}}_{= 0 \text{ (anti-symmetric argument)}}$$

$$= \sum_i P_i V_i \sum_j (\boldsymbol{u}_j - \boldsymbol{u}_i) \cdot \boldsymbol{\nabla}_i W_{ij} V_j = \sum_i P_i \left[\frac{dV_i}{dt} - \boldsymbol{\Theta}_{i,Rie}^V - V_i \sum_j (\delta\boldsymbol{u}_j - \delta\boldsymbol{u}_i) \cdot \boldsymbol{\nabla}_i W_{ij} V_j \right] \tag{A.3}$$

where the last equality is obtained by substituting the continuity equation of the system (3) (namely, the second equation of the system). Since $V_i = m_i/\rho_i$, the first term in the right-hand side is rearranged as follows:

$$\sum_i P_i \frac{dV_i}{dt} = -\sum_i m_i \frac{P_i}{\rho_i^2} \frac{d\rho_i}{dt} + \sum_i \frac{P_i}{\rho_i} \frac{dm_i}{dt} = -\sum_i m_i \frac{de_i}{dt} + \sum_i \frac{P_i}{\rho_i} \frac{dm_i}{dt} = -\frac{d\mathcal{E}_C}{dt} + \sum_i \left(\frac{P_i}{\rho_i} + e_i \right) \frac{dm_i}{dt}.$$

Substituting the above equality in the expression of ①, we obtain:

$$① = -\frac{d\mathcal{E}_C}{dt} + \overbrace{\sum_i \left(\frac{P_i}{\rho_i} + e_i \right) \frac{dm_i}{dt}}^{⑦} \overbrace{-\sum_i P_i \boldsymbol{\Theta}_{i,Rie}^V}^{⑧} \overbrace{-\sum_i P_i V_i \sum_j (\delta\boldsymbol{u}_j - \delta\boldsymbol{u}_i) \cdot \boldsymbol{\nabla}_i W_{ij} V_j}^{⑨}. \tag{A.4}$$

Using the decomposition in symmetric and anti-symmetric parts, it easy to prove that the terms ⑧ and ⑨ correspond to the expressions (31) and (33) respectively. About the term ⑦, this contains the specific enthalpy of the particle, namely $h_i = P_i/\rho_i + e_i$, and the time derivative of the particle mass which is expressed, as usual, through the third equation in the system (3). Hence, we obtain:

$$⑦ = \frac{1}{2} \sum_i \sum_j (h_i - h_j)(\rho_i \delta\boldsymbol{u}_i + \rho_j \delta\boldsymbol{u}_j) \cdot \boldsymbol{\nabla}_i W_{ij} V_j V_j \tag{A.5}$$

Using the definition of e_i in Eq. (29), it easy to prove that the term ⑦ corresponds to the expression (36). Collecting in Eq. (A.4) all the above contributions, we obtain:

$$① = -\frac{d\mathcal{E}_C}{dt} + \mathcal{P}_{\delta\boldsymbol{u}}^{m,2} + \mathcal{P}_{Rie}^{cont} + \mathcal{P}_{\delta\boldsymbol{u}}^{cont} \tag{A.6}$$

Finally, substituting this expression in Eq. (A.2), we find the equation of the energy balance for the *QL-ALE* scheme.

Regarding the term ②, when $\boldsymbol{f}_i$ is a conservative force derived from the potential Φ_i (i.e. $\boldsymbol{f}_i = \boldsymbol{\nabla}\Phi_i$), it is possible to introduce the potential energy $\mathcal{E}_p = -\sum_i m_i \Phi_i$. In that case, using Eq. (7), we obtain

$$\frac{d(m_i \Phi_i)}{dt} = \frac{dm_i}{dt} \Phi_i + m_i \frac{d\Phi_i}{dt} = \frac{dm_i}{dt} \Phi_i + m_i(\boldsymbol{u}_i + \delta\boldsymbol{u}_i) \cdot \boldsymbol{\nabla}\Phi_i$$

and then:

$$\mathcal{P}_f := \sum_i m_i \boldsymbol{u}_i \cdot \boldsymbol{f}_i = -\frac{d\mathcal{E}_p}{dt} - \frac{dm_i}{dt} \Phi_i - m_i \delta\boldsymbol{u}_i \cdot \boldsymbol{f}_i \tag{A.7}$$

leading to the energy balance in Eq. (40).

Appendix B. Energy balance for the *QL-MassCons* scheme: details of computation

For the derivation of the energy balance for the *QL-MassCons* scheme we apply the same approach described in the previous section for *QL-ALE* scheme. In any case, two main differences appear. The first difference regards the particle masses, which are constant during the evolution. This implies that the terms ⑥ and ⑦ of the previous section are identically null, as well as the related terms (35) and (36). The second difference regards the PST contributions in the volume equation of the system (9). Indeed, these differ from the corresponding part in the volume equation of the *QL-ALE* scheme and, consequently, lead to a different contribution in the term ① of the Eq. (A.3) and to a different expression for $\mathcal{P}_{\delta\boldsymbol{u}}^{cont}$ [see Eq. (37)]. All the remaining terms are identical to the *QL-ALE* scheme.

Incidentally, we highlight a further interesting aspect about the term $\mathcal{P}_{\delta u}^{cont}$ of the *QL-MassCons* model. Summing up the terms ⑦ and ⑨, respectively $\mathcal{P}_{\delta u}^{m,2}$ and $\mathcal{P}_{\delta u}^{cont}$ of the *QL-ALE* scheme, we obtain the following expression:

$$
\begin{aligned}
\mathcal{P}_{\delta u}^{cont} + \mathcal{P}_{\delta u}^{m,2} &= \frac{1}{2} \sum_i \sum_j \left[-(P_i + P_j)\left(\delta \boldsymbol{u}_j - \delta \boldsymbol{u}_i\right) + (h_i - h_j)\left(\rho_i \delta \boldsymbol{u}_i + \rho_j \delta \boldsymbol{u}_j\right)\right] \cdot \boldsymbol{\nabla}_i W_{ij} V_i V_j \\
&= \frac{1}{2} \sum_i \sum_j \left[-(P_i + P_j)\left(\delta \boldsymbol{u}_j - \delta \boldsymbol{u}_i\right) + \left(\frac{P_i}{\rho_i} - \frac{P_j}{\rho_j}\right)\left(\rho_i \delta \boldsymbol{u}_i + \rho_j \delta \boldsymbol{u}_j\right)\right] \cdot \boldsymbol{\nabla}_i W_{ij} V_i V_j \\
&\quad + \frac{1}{2} \sum_i \sum_j (e_i - e_j)\left(\rho_i \delta \boldsymbol{u}_i + \rho_j \delta \boldsymbol{u}_j\right) \cdot \boldsymbol{\nabla}_i W_{ij} V_i V_j
\end{aligned}
\tag{B.1}
$$

whose first contribution in the right-hand side coincides with the term $\mathcal{P}_{\delta u}^{cont}$ of the *QL-MassCons* [see Eq. (37)]. Since $\mathcal{P}_{\delta u}^{m,2}$ comes from the mass equation of the *QL-ALE* scheme, this suggests that a sort of 'trace' of the mass variation is hidden in the *QL-MassCons* scheme, even though in the latter model m_i is constant during the evolution. Using different words and a different perspective, this suggests that the volume equation of the *QL-MassCons* scheme preserves a trace of the variation caused by the evolution of the particles' masses.

Appendix C. Leading orders in the PST terms

In this section we highlight the leading orders of the PST terms in the continuity equation and in the energy balance.

C.1. PST in the continuity equation

Volume, density and mass of a generic particle are related through the usual relation $m_i = \rho_i V_i$. Hence, applying a time derivative we obtain:

$$
\frac{d\rho_i}{dt} = \frac{1}{V_i}\left[\frac{dm_i}{dt} - \rho_i \frac{dV_i}{dt}\right],
\tag{C.1}
$$

that is used to recover the equation for the evolution of the density (i.e., the continuity equation). After some algebra, it is simple to show that both the *QL-ALE* and the *QL-MassCons* schemes are governed by the same equation, namely:

$$
\frac{d\rho_i}{dt} = -\rho_i \sum_j \left(\boldsymbol{u}_j - \boldsymbol{u}_i\right) \cdot \boldsymbol{\nabla}_i W_{ij} \, V_j - \rho_i \frac{\Theta_{Rie}^V}{V_i} + \sum_j (\rho_j - \rho_i)\delta \boldsymbol{u}_j \cdot \boldsymbol{\nabla}_i W_{ij} V_j + 2\rho_i \delta \boldsymbol{u}_i \cdot \boldsymbol{\nabla} \Gamma_i.
$$

where

$$
\boldsymbol{\nabla}\Gamma_i = \sum_j \boldsymbol{\nabla}_i W_{ij} Vj
\tag{C.2}
$$

As shown in the Appendix D, $\Theta_{Rie}^V / V_i = \mathcal{O}(R^2)$ and, therefore, it is negligible in comparison to the other terms. Similarly, $(\rho_j - \rho_i)$ is negligible because of the weak-compressibility assumption. Hence, the leading order terms in the continuity equation are:

$$
\frac{d\rho_i}{dt} \approx \underbrace{-\rho_i \sum_j \left(\boldsymbol{u}_j - \boldsymbol{u}_i\right) \cdot \boldsymbol{\nabla}_i W_{ij} \, V_j}_{\text{Lagrangian part}} + \underbrace{2\rho_i \delta \boldsymbol{u}_i \cdot \boldsymbol{\nabla}\Gamma_i}_{\text{PST part}}
\tag{C.3}
$$

Some remarks can be drawn for the leading-order PST term in Eq. (C.3):

- in the SPH literature the greatest part of PST velocities satisfy the condition $\delta \boldsymbol{u}_i \sim -\boldsymbol{\nabla}\Gamma_i$ by construction. This implies that $\delta \boldsymbol{u}_i \cdot \boldsymbol{\nabla}\Gamma_i \lesssim 0$, leading to a negative definite contribution in the density equation.
- when the particle distribution is uniform, $\boldsymbol{\nabla}\Gamma_i \simeq 0$ and the last term in the right-hand side of Eq. (C.3) is, in fact, negligible. On the contrary, if the particle distribution is not uniform, $\boldsymbol{\nabla}\Gamma_i = \mathcal{O}(1/\Delta x)$ (see, for example, [62]), while the PST velocity generally satisfies $\delta \boldsymbol{u}_i = \mathcal{O}(\Delta x)$. This implies $\delta \boldsymbol{u}_i \cdot \boldsymbol{\nabla}\Gamma_i = \mathcal{O}(1)$.

C.2. PST in the energy balance

As shown in Appendices A and B, the contribution coming from the PST in the energy balance of the *QL-ALE* and *QL-MassCons* schemes are slightly different because of the variation of the mass in the former scheme. In both the cases, however, the leading orders come from the continuity equation because of the presence of contributions proportional to $\nabla \Gamma_i$, while the terms $\mathcal{P}_{\delta u}^{mom}$ and $\mathcal{P}_{\delta u}^{m,1}$ represent secondary contributions. This is shown below.

Considering the *QL-ALE* scheme, the overall contribution is given by Eq. (B.1) and can be rearranged as follows:

$$\mathcal{P}_{\delta u}^{cont} + \mathcal{P}_{\delta u}^{m,2} = \sum_i \sum_j \left(P_i \delta u_i - P_j \delta u_j \right) \cdot \nabla_i W_{ij} V_i V_j$$

$$+ \frac{1}{2} \sum_i \sum_j \left[(\rho_j - \rho_i) \left(\frac{P_i}{\rho_i} \delta u_j + \frac{P_j}{\rho_j} \delta u_i \right) + (e_i - e_j) \left(\rho_i \delta u_i + \rho_j \delta u_j \right) \right] \cdot \nabla_i W_{ij} V_i V_j .$$

The last term in the right-hand side plays a minor role, since both $(\rho_j - \rho_i)$ and $(e_i - e_j)$ are small because of the weak-compressibility assumption. On the contrary, the first term represents the leading-order contribution of the PST to the energy balance. In fact, substituting $(P_i \delta u_i - P_j \delta u_j) = 2 P_i \delta u_i - (P_i \delta u_i + P_j \delta u_j)$ and simplifying the anti-symmetric contribution, we obtain:

$$\mathcal{P}_{\delta u}^{cont} + \mathcal{P}_{\delta u}^{m,2} \approx 2 \sum_i V_i P_i \delta u_i \cdot \nabla \Gamma_i .$$

The same procedure applies to the *QL-MassCons* scheme, leading to the same result.

Appendix D. Leading-order expressions for the Riemann term

Here we derive the expansions for the diffusive terms of the Riemann-SPH model at the continuum. Under the weakly-compressibility assumption, we simplify them by assuming that the variations of the sound velocity and of the density are negligible, that is $c_L = c_R = c_0$ and $\rho_L = \rho_R = \rho_0$. Then, the expressions (12) and (13) with the Riemann fluxes given by the Eqs. (18) and (19) become:

$$\theta_{Rie}^V = - \left[\left(u' + u - u_R - u_L \right) \cdot \frac{(x' - x)}{\|x' - x\|} + \frac{P_R - P_L}{\rho_0 c_0} \right] \frac{(x' - x)}{\|x' - x\|} \tag{D.1}$$

$$\theta_{Rie}^{V\rho u} = - \left[\left(P' + P - P_R - P_L \right) + \rho_0 c_0 \left(u_R - u_L \right) \cdot \frac{(x' - x)}{\|x' - x\|} \right] , \tag{D.2}$$

where the apex indicates the quantities evaluated at x'. We assume that all the fluid fields are sufficiently smooth and that there are no boundaries (namely, no kernel truncation). Under this hypothesis, the reconstruction of a generic fluid field f at the mid point between the point x and x' reads

$$f_L = f + \frac{1}{2} \frac{\partial f}{\partial x_i} (x' - x)_i , \qquad f_R = f' - \frac{1}{2} \frac{\partial f'}{\partial x_i'} (x' - x)_i , \tag{D.3}$$

From the Eqs. (D.1) and (D.2) we find two different kernels that has to be studied, namely:

$$N_1 = f_R - f_L , \qquad N_2 = f' + f - f_R - f_L , \tag{D.4}$$

and from Eq. (D.3), it follows:

$$N_1 = (f' - f) - \frac{1}{2} \left(\frac{\partial f'}{\partial x_i'} + \frac{\partial f}{\partial x_i} \right) (x' - x)_i , \qquad N_2 = \frac{1}{2} \left(\frac{\partial f'}{\partial x_i'} - \frac{\partial f}{\partial x_i} \right) (x' - x)_i .$$

Remarkably, the kernel N_1 is exactly the argument of the diffusive term of the δ-SPH (see for example [63]). As a consequence, for this case we can use the results shown in the equation (A.8) of [63] and write:

$$N_1 = - \frac{1}{12} \left(\frac{\partial^3 f}{\partial x_i \partial x_j \partial x_k} \right) \Delta_i \Delta_j \Delta_k - \frac{1}{24} \left(\frac{\partial^4 f}{\partial x_i \partial x_j \partial x_k \partial x_l} \right) \Delta_i \Delta_j \Delta_k \Delta_l + \mathcal{O} \left(\|\Delta\|^5 \right) ,$$

where $\Delta = (x' - x)$. Conversely, the kernel N_2 has the following expansion:

$$N_2 = \frac{1}{2} \left(\frac{\partial^2 f}{\partial x_i \partial x_j} \right) \Delta_i \Delta_j + \frac{1}{4} \left(\frac{\partial^3 f}{\partial x_i \partial x_j \partial x_k} \right) \Delta_i \Delta_j \Delta_k + \mathcal{O} \left(\|\Delta\|^4 \right) , \tag{D.5}$$

When these expansions are substituted inside θ^V_{Rie} and, then, in $\Theta^V_{i,j,Rie}$, we obtain:

$$
\frac{\Theta^V_{Rie}}{V_0} = -\int \left[(\boldsymbol{u}' + \boldsymbol{u} - \boldsymbol{u}_R - \boldsymbol{u}_L) \cdot \frac{(\boldsymbol{x}' - \boldsymbol{x})}{\|\boldsymbol{x}' - \boldsymbol{x}\|} \right] \frac{(\boldsymbol{x}' - \boldsymbol{x})}{\|\boldsymbol{x}' - \boldsymbol{x}\|} \cdot \nabla W \, dV' - \int \frac{(P_R - P_L)}{c_0 \rho_0} \frac{(\boldsymbol{x}' - \boldsymbol{x})}{\|\boldsymbol{x}' - \boldsymbol{x}\|} \cdot \nabla W \, dV'
$$

$$
= -\frac{R^2}{4} \left(\frac{\partial^3 u_i}{\partial x_j \partial x_k \partial x_l} \right) \mathbb{M}_{i,j,k,l} + \frac{1}{c_0 \rho_0} \frac{R^3}{24} \left(\frac{\partial^4 P}{\partial x_i \partial x_j \partial x_k \partial x_l} \right) \mathbb{N}_{i,j,k,l} + \mathcal{O}\left(R^4\right) ,
$$

where V_0 is the reference volume (namely, $V_0 = \Delta x^n$) and:

$$
\mathbb{M}_{i,j,k,l} = -\int \frac{q_i\, q_j\, q_k\, q_l}{q} \frac{\partial W}{\partial q} \, dV' , \quad \mathbb{N}_{i,j,k,l} = -\int q_i\, q_j\, q_k\, q_l \frac{\partial W}{\partial q} \, dV' , \tag{D.6}
$$

and $\vec{q} = (\boldsymbol{x}' - \boldsymbol{x})/R$, $q = \|\vec{q}\|$ and the kernel function is assumed to depend only on q, namely $W = W(q)$. Note that the leading order terms in the expansions of N_1 and N_2 cancels out because of the radial symmetry of the kernel function. Following [64], we decompose the tensors $\mathbb{M}$ and $\mathbb{N}$ as below:

$$
\mathbb{M}_{i,j,k,l} = \frac{\alpha}{2} \left[\delta_{ik}\delta_{jl} + \delta_{il}\delta_{jk} + \delta_{ij}\delta_{kl} \right] , \quad \mathbb{N}_{i,j,k,l} = \frac{\beta}{2} \left[\delta_{ik}\delta_{jl} + \delta_{il}\delta_{jk} + \delta_{ij}\delta_{kl} \right]
$$

where

$$
\alpha = -\frac{2}{3} \int \frac{q_i^4}{q} \frac{\partial W}{\partial q} \, dV' , \quad \beta = -\frac{2}{3} \int q_i^4 \frac{\partial W}{\partial q} \, dV' . \tag{D.7}
$$

Note that both α and β are positive because $\partial W / \partial q$ is negative. Using the above results, we obtain:

$$
\frac{\Theta^V_{Rie}}{V_0} = -\frac{3\,R^2}{8} \alpha\, \Delta\,(\nabla \cdot \boldsymbol{u}) + \frac{1}{c_0 \rho_0} \frac{R^3}{16} \beta\, \Delta^2 P + \mathcal{O}\left(R^4\right) , \tag{D.8}
$$

About $\boldsymbol{\Theta}^{V\rho\boldsymbol{u}}_{Rie}$, we find:

$$
\frac{\boldsymbol{\Theta}^{V\rho\boldsymbol{u}}_{Rie}}{V_0} = \int \left(P' + P - P_R - P_L \right) \nabla W \, dV' + \rho_0\, c_0 \int (\boldsymbol{u}_R - \boldsymbol{u}_L) \cdot \frac{(\boldsymbol{x}' - \boldsymbol{x})}{\|\boldsymbol{x}' - \boldsymbol{x}\|} \nabla W \, dV'
$$

$$
= \frac{R^2}{8} \left(\frac{\partial^3 P}{\partial x_j \partial x_k \partial x_l} \right) \mathbb{M}_{i,j,k,l} - \rho_0\, c_0 \frac{R^3}{24} \left(\frac{\partial^4 u_j}{\partial x_k \partial x_l \partial x_m \partial x_n} \right) \mathbb{G}_{i,j,k,l,m,n} + \mathcal{O}\left(R^4\right) ,
$$

where:

$$
\mathbb{G}_{i,j,k,l,m,n} = -\int \frac{q_i\, q_j\, q_k\, q_l\, q_m\, q_n}{q^2} \frac{\partial W}{\partial q} \, dV' . \tag{D.9}
$$

Using the results above and those described in the Appendix D.1 for the tensor $\mathbb{G}$, we obtain:

$$
\frac{\boldsymbol{\Theta}^{V\rho\boldsymbol{u}}_{Rie}}{V_0} = \frac{3R^2}{8} \alpha\, \nabla\,(\Delta P) - \rho_0\, c_0 \frac{R^3}{120} \gamma \left[\Delta^2 \boldsymbol{u} + 4\, \nabla\,(\Delta\,(\nabla \cdot \boldsymbol{u})) \right] + \mathcal{O}\left(R^4\right) ,
$$

where

$$
\gamma = -\int \frac{q_i^6}{q^2} \frac{\partial W}{\partial q} \, dV' . \tag{D.10}
$$

D.1. The sixth-order tensor $\mathbb{G}$

Along with γ in Eq. (D.10), we define the following parameters:

$$
\eta = -\int \frac{q_i^4\, q_j^2}{q^2} \frac{\partial W}{\partial q} \, dV' \quad \text{with} \quad i \neq j , \qquad \text{and} \qquad \xi = -\int \frac{q_i^2\, q_j^2\, q_k^2}{q^2} \frac{\partial W}{\partial q} \, dV' \quad \text{with} \quad i \neq j \neq k .
$$

To compute the relations among γ, η and ξ we follow the same approach described in [65]. Since the tensor $\mathbb{G}$ is invariant under rigid rotations by definition, we consider a rotation with angle $\pi/4$ along the z-axis and write the following identity:

$$
\int \frac{x^6}{q^2} \frac{\partial W}{\partial q} \, dV' = \int \left(\frac{\hat{x} + \hat{y}}{\sqrt{2}} \right)^6 \frac{1}{q^2} \frac{\partial W}{\partial q} \, dV' \tag{D.11}
$$

where the variables with the hat are the coordinates in the rotated frame of reference. Expanding and removing the odd orders (which cancel out because of the radial symmetry of the kernel function), we obtain $\gamma = 5\,\eta$. Then, we consider a rotation of $\pi/4$ along the z-axis and a rotation of $\pi/4$ along the y-axis and obtain the following identity:

$$\int \frac{x^6}{q^2} \frac{\partial W}{\partial q}\, dV' = \int \left(\frac{\hat{x}}{2} + \frac{\hat{y}}{2} + \frac{\hat{z}}{\sqrt{2}} \right)^6 \frac{1}{q^2} \frac{\partial W}{\partial q}\, dV', \tag{D.12}$$

and, expanding and using the relation between γ and η, we obtain $\gamma = 15\,\xi$.

Now, we consider the following tensor product:

$$\left(\frac{\partial^4 u_j}{\partial x_k \partial x_l \partial x_m \partial x_n} \right) \mathbb{G}_{i,j,k,l,m,n}. \tag{D.13}$$

To simplify the computations, we fix the ith component, that is a specific direction of the coordinates system. In particular, we choose $i = 1$ and write all the non-null combinations of the indices. The simplest case is given by:

five times '1'	j	k	l	m	n	coefficient	terms
	1	1	1	1	1	γ	$\dfrac{\partial^4 u}{\partial x^4}$

Then, we consider:

three times '1', two times '2'	j	k	l	m	n	coefficient	terms
permutations of	1	1	1	2	2	η	$6\dfrac{\partial^4 u}{\partial x^2 \partial y^2} + 4\dfrac{\partial^4 v}{\partial x^3 \partial y}$

along with the symmetric case when '2' is replaced by '3'. The subsequent case is given by:

one time '1', four times '2'	j	k	l	m	n	coefficient	terms
permutations of	1	2	2	2	2	η	$\dfrac{\partial^4 u}{\partial y^4} + 4\dfrac{\partial^4 v}{\partial x \partial y^3}$

along with the symmetric case when '2' is replaced by '3'. Finally, we consider:

two times '2' and '3' (j fixed)	k	l	m	n	coefficient	terms
j=1 fixed, permutations of	2	2	3	3	ξ	$6\dfrac{\partial^4 u}{\partial y^2 \partial z^2}$
j=2 fixed, permutations of	1	2	3	3	ξ	$12\dfrac{\partial^4 v}{\partial x \partial y \partial z^2}$
j=3 fixed, permutations of	1	2	2	3	ξ	$12\dfrac{\partial^4 w}{\partial x \partial y^2 \partial z}$

Collecting all the contributions together, we find:

$$\left(\frac{\partial^4 u_j}{\partial x_k \partial x_l \partial x_m \partial x_n} \right) \mathbb{G}_{i,j,k,l,m,n} = \gamma\, \frac{\partial^4 u}{\partial x^4} + 6\,\eta\, \frac{\partial^4 u}{\partial x^2 \partial y^2} + 4\,\eta\, \frac{\partial^4 v}{\partial x^3 \partial y} + 6\,\eta\, \frac{\partial^4 u}{\partial x^2 \partial z^2} + 4\,\eta\, \frac{\partial^4 w}{\partial x^3 \partial z}$$
$$+\eta\, \frac{\partial^4 u}{\partial y^4} + 4\,\eta\, \frac{\partial^4 v}{\partial x \partial y^3} + \eta\, \frac{\partial^4 u}{\partial z^4} + 4\,\eta\, \frac{\partial^4 w}{\partial x \partial z^3} + 6\,\xi\, \frac{\partial^4 u}{\partial y^2 \partial z^2} + 12\,\xi\, \frac{\partial^4 v}{\partial x \partial y \partial z^2} + 12\,\xi\, \frac{\partial^4 w}{\partial x \partial y^2 \partial z}$$

which holds true for $i = 1$. Then, substituting the expression for η and ξ as functions of γ and generalizing for a generic ith component, we obtain:

$$\left(\frac{\partial^4 u_j}{\partial x_k \partial x_l \partial x_m \partial x_n} \right) \mathbb{G}_{i,j,k,l,m,n} = \frac{\gamma}{5} \left[\Delta^2 \boldsymbol{u} + 4\,\nabla\left(\Delta\left(\nabla \cdot \boldsymbol{u} \right) \right) \right].$$

References

[1] J.J. Monaghan, On the problem of penetration in particle methods, J. Comput. Phys. 82 (1989).

[2] S.J. Lind, R. Xu, P.K. Stansby, B.D. Rogers, Incompressible smoothed particle hydrodynamics for free-surface flows: A generalised diffusion-based algorithm for stability and validations for impulsive flows and propagating waves, J. Comput. Phys. 231 (4) (2012) 1499–1523.

[3] G. Oger, S. Marrone, D. Le Touzé, M. De Leffe, SPH accuracy improvement through the combination of a quasi-Lagrangian shifting transport velocity and consistent ALE formalisms, J. Comput. Phys. 313 (2016) 76–98.

[4] P.N. Sun, A. Colagrossi, S. Marrone, A.M. Zhang, The δ-plus-SPH model: Simple procedures for a further improvement of the SPH scheme, Comput. Methods Appl. Mech. Engrg. 315 (2017) 25–49.

[5] L. Chiron, G. Oger, M. De Leffe, D. Le Touzé, Analysis and improvements of adaptive particle refinement (APR) through CPU time, accuracy and robustness considerations, J. Comput. Phys. 354 (2018) 552–575.

[6] P.N. Sun, A. Colagrossi, S. Marrone, M. Antuono, A.-M. Zhang, A consistent approach to particle shifting in the δ-plus-SPH model, Comput. Methods Appl. Mech. Engrg. 348 (2019) 912–934.

[7] J. Michel, Développements numériques de la méthode SPH couplée aux Eléments Finis appliqués au phénomène de l'hydroplanage (Ph. D thesis), Ecole Centrale de Nantes, 2020.

[8] J. Michel, G. Oger, D. Le Touzé, Effects of particle disordering on local and global fluid volume in the SPH method and proposition of an improved SPH-ale scheme, in: Proceedings of the 13th International SPHERIC Workshop, 2018, pp. 275–282.

[9] J.-P. Vila, On particle weighted methods and smooth particle hydrodynamics, Math. Models Methods Appl. Sci. 9 (2) (1999) 161–209.

[10] M. Antuono, P.N. Sun, S. Marrone, A. Colagrossi, The δ-ALE-SPH model: An arbitrary Lagrangian–Eulerian framework for the δ-SPH model with particle shifting technique, Comput. & Fluids 216 (2021) 104806.

[11] J.-C. Marongiu, F. Leboeuf, J. Caro, E. Parkinson, Free surface flows simulations in pelton turbines using an hybrid SPH-ALE method, J. Hydraul. Res. 48 (S1) (2010) 40–49.

[12] P.K. Koukouvinis, J.S. Anagnostopoulos, D.E. Papantonis, An improved MUSCL treatment for the SPH-ALE method: comparison with the standard SPH method for the jet impingement case, Internat. J. Numer. Methods Fluids 71 (9) (2013) 1152–1177.

[13] A.N. Parshikov, S.A. Medin, Smoothed Particle Hydrodynamics using interparticle contact algorithms, J. Comp. Phys. 180 (2002) 358–382.

[14] B. Bouscasse, A. Colagrossi, A. Souto-Iglesias, J.L. Cercos-Pita, Mechanical energy dissipation induced by sloshing and wave breaking in a fully coupled angular motion system. i. Theoretical formulation and numerical investigation, Phys. Fluids 26 (3) (2014) 033103.

[15] J. Martinez-Carrascal, L.M. González-Gutiérrez, Experimental study of the liquid damping effects on a SDOF vertical sloshing tank, J. Fluids Struct. 100 (2021) 103172.

[16] M. Antuono, S. Marrone, A. Colagrossi, B. Bouscasse, Energy balance in the δ-SPH scheme, Comput. Methods Appl. Mech. Engrg. 289 (2015) 209–226.

[17] J.L. Cercos-Pita, R.A. Dalrymple, A. Herault, Diffusive terms for the conservation of mass equation in {SPH}, Appl. Math. Model. 40 (19) (2016) 8722–8736.

[18] J.L. Cercos-Pita, M. Antuono, A. Colagrossi, A. Souto-Iglesias, SPH energy conservation for fluid–solid interactions, Comput. Methods Appl. Mech. Engrg. 317 (2017) 771–791.

[19] C. Hermange, G. Oger, D. Le Touzé, Energy considerations in the SPH method with deformable boundaries and application to FSI problems, J. Comput. Phys. X 1 (2019) 100008.

[20] D.D. Meringolo, Y. Liu, X.-Y. Wang, A. Colagrossi, Energy balance during generation, propagation and absorption of gravity waves through the δ-LES-SPH model, Coast. Eng. 140 (2018) 355–370.

[21] A. Khayyer, H. Gotoh, Y. Shimizu, K. Gotoh, On enhancement of energy conservation properties of projection-based particle methods, Eur. J. Mech. B/Fluids 66 (2017) 20–37.

[22] J. Michel, A. Vergnaud, G. Oger, C. Hermange, D. Le Touzé, On Particle Shifting Techniques (PSTs): Analysis of existing laws and proposition of a convergent and multi-invariant law, J. Comput. Phys. (2022) 110999.

[23] G. Bulian, A. Souto-Iglesias, L. Delorme, E. Botia-Vera, SPH simulation of a tuned liquid damper with angular motion, J. Hydraul. Res. 48 (Extra Issue) (2010) 28–39.

[24] A. Marsh, M. Prakash, E. Semercigil, Ö.F. Turan, A numerical investigation of energy dissipation with a shallow depth sloshing absorber, Appl. Math. Model. 34 (10) (2010) 2941–2957.

[25] S. Marrone, A. Colagrossi, A. Di Mascio, D. Le Touzé, Analysis of free-surface flows through energy considerations: Single-phase versus two-phase modeling, Phys. Rev. E 93 (2016) 053113.

[26] Z. Wei, R.A. Dalrymple, Surf zone wave heating by energy dissipation of breaking waves, Coast. Eng. Proc. 36 (2018) 1–14.

[27] S. Marrone, A. Colagrossi, A. Di Mascio, D. Le Touzé, Prediction of energy losses in water impacts using incompressible and weakly compressible models, J. Fluids Struct. 54 (2015) 802–822.

[28] M. Antuono, A. Colagrossi, S. Marrone, Numerical diffusive terms in weakly-compressible SPH schemes, Comput. Phys. Comm. 183 (12) (2012) 2570–2580.

[29] I. Hammani, S. Marrone, A. Colagrossi, G. Oger, D. Le Touzé, Detailed study on the extension of the δ-SPH model to multi-phase flow, Comput. Methods Appl. Mech. Engrg. 368 (2020) 113189.

[30] M.D. Green, R. Vacondio, J. Peiró, A smoothed particle hydrodynamics numerical scheme with a consistent diffusion term for the continuity equation, Comput. & Fluids 179 (2019) 632–644.

[31] C. Zhang, X.Y. Hu, N.A. Adams, A weakly compressible SPH method based on a low-dissipation Riemann solver, J. Comput. Phys. 335 (2017) 605–620.

[32] C. Zhang, G.M. Xiang, B. Wang, X.Y. Hu, N.A. Adams, A weakly compressible SPH method with WENO reconstruction, J. Comput. Phys. 392 (2019) 1–18.

[33] Z.-F. Meng, A.-M. Zhang, P.-P. Wang, F.-R. Ming, B.C. Khoo, A targeted essentially non-oscillatory (TENO) SPH method and its applications in hydrodynamics, Ocean Eng. 243 (2022) 110100.

[34] Zi-Fei Meng, A-Man Zhang, Ping-Ping Wang, Fu-Ren Ming, A shock-capturing scheme with a novel limiter for compressible flows solved by smoothed particle hydrodynamics, Comput. Methods Appl. Mech. Engrg. 386 (2021) 114082.

[35] A. Khayyer, H. Gotoh, Y. Shimizu, Comparative study on accuracy and conservation properties of two particle regularization schemes and proposal of an optimized particle shifting scheme in ISPH context, J. Comput. Phys. 332 (2017) 236–256.

[36] Z. Li, J. Leduc, A. Combescure, F. Leboeuf, Coupling of SPH-ALE method and finite element method for transient fluid–structure interaction, Comput. & Fluids 103 (2014) 6–17.

[37] D.D. Meringolo, S. Marrone, A. Colagrossi, Y. Liu, A dynamic δ-SPH model: How to get rid of diffusive parameter tuning, Comput. & Fluids 179 (2019) 334–355.

[38] A. Collé, J. Limido, J.-P. Vila, An accurate multi-regime SPH scheme for barotropic flows, J. Comput. Phys. 388 (2019) 561–600.

[39] P.-P. Wang, Z.-F. Meng, A.-M. Zhang, F.-R. Ming, P.-N. Sun, Improved particle shifting technology and optimized free-surface detection method for free-surface flows in smoothed particle hydrodynamics, Comput. Methods Appl. Mech. Engrg. 357 (2019) 112580.

[40] A. Vergnaud, G. Oger, D. Le Touzé, M. DeLeffe, C-CSF: Accurate, robust and efficient surface tension and contact angle models for single-phase flows using SPH, Comput. Methods Appl. Mech. Engrg. 389 (2022) 114292.

[41] S. Marrone, A. Colagrossi, F. Gambioli, L. González-Gutiérrez, Numerical study on the dissipation mechanisms in sloshing flows induced by violent and high-frequency accelerations. I. Theoretical formulation and numerical investigation, Phys. Rev. Fluids 6 (2021) 114801.

[42] Alban Vergnaud, Guillaume Oger, David. Le Touzé, Investigations on a high order sph scheme using weno reconstruction, J. Comput. Phys. (2023) 111889.

[43] M. Antuono, S. Marrone, A. Di Mascio, A. Colagrossi, Smoothed particle hydrodynamics method from a large eddy simulation perspective. Generalization to a quasi-Lagrangian model, Phys. Fluids 33 (1) (2021) 015102.

[44] H. Wendland, Piecewise polynomial, positive definite and compactly supported radial functions of minimal degree, Adv. Comput. Math. 4 (4) (1995) 389–396.

[45] S. Adami, X.Y. Hu, N.A. Adams, A transport-velocity formulation for smoothed particle hydrodynamics, J. Comput. Phys. 241 (2013) 292–307.

[46] J.J. Monaghan, SPH and Riemann solvers, J. Comput. Phys. 136 (2) (1997) 298–307.

[47] S. Inutsuka, Reformulation of smoothed particle hydrodynamics with Riemann solver, J. Comput. Phys. 179 (2002) 238–2667.

[48] K. Puri, P. Ramachandran, Approximate Riemann solvers for the Godunov SPH (GSPH), J. Comput. Phys. 270 (2014) 432–458.

[49] Z.-F. Meng, A.-M. Zhang, J.-L. Yan, P.-P. Wang, A. Khayyer, A hydroelastic fluid–structure interaction solver based on the Riemann-SPH method, Comput. Methods Appl. Mech. Engrg. 390 (2022) 114522.

[50] A.N. Parshikov, Application of a solution to the Riemann problem in the SPH method, Comput. Math. Math. Phys. 39 (1999) 1216–1225.

[51] G. Murante, S. Borgani, R. Brunino, S.-H. Cha, Hydrodynamic simulations with the Godunov smoothed particle hydrodynamics, Mon. Not. R. Astron. Soc. 417 (1) (2011) 136–153, 10.

[52] B. Van Leer, Towards the ultimate conservative difference scheme. V. A second-order sequel to Godunov's method, J. Comput. Phys. 32 (1) (1979) 101–136.

[53] E.F. Toro, Riemann Solvers and Numerical Methods for Fluid Dynamics: A Practical Introduction, Springer Science & Business Media, 2013.

[54] J. Michel, M. Antuono, S. Marrone, G. Oger, Analysis through energy consideration of a quasi-lagrangian scheme using riemann stabilization, in: 16th Int. SPHERIC Workshop, June, 7-9, 2022.

[55] S. Marrone, A. Colagrossi, D. Le Touzé, G. Graziani, Fast free-surface detection and level-set function definition in SPH solvers, J. Comput. Phys. 229 (10) (2010) 3652–3663.

[56] A. Colagrossi, D. Durante, J. Bonet Avalos, A. Souto-Iglesias, Discussion of Stokes' hypothesis through the smoothed particle hydrodynamics model, Phys. Rev. E 96 (2017) 023101.

[57] G. Taylor, A.E. Green, Mechanism of the production of small eddies from large ones, Proc. R. Soc. A 158 (1937) 499–521.

[58] A. Colagrossi, B. Bouscasse, M. Antuono, S. Marrone, Particle packing algorithm for SPH schemes, Comput. Phys. Comm. 183 (2) (2012) 1641–1683.

[59] J.J. Monaghan, A. Rafiee, A simple SPH algorithm for multi-fluid flow with high density ratios, Internat. J. Numer. Methods Fluids 71 (5) (2013) 537–561.

[60] W.G. Szymczak, Energy losses in non-classical free surface flows, in: J.R. Blake, J.M. Boulton-Stone, N.H. Thomas (Eds.), Bubble Dynamics and Interface Phenomena, in: Fluid Mechanics and Its Applications, vol. 23, Springer Netherlands, 1994, pp. 413–420.

[61] M.J. Cooker, Liquid impact, kinetic energy loss and compressibility: Lagrangian, Eulerian and acoustic viewpoints, J. Eng. Math. 44 (3) (2002) 259–276.

[62] N.J. Quinlan, M. Lastiwka, M. Basa, Truncation error in mesh-free particle methods, Internat. J. Numer. Methods Engrg. 66 (13) (2006) 2064–2085.

[63] M. Antuono, A. Colagrossi, The damping of viscous gravity waves, Wave Motion 50 (2012) 197–209.

[64] M. Moakher, Fourth-order cartesian tensors: old and new facts, notions and applications, Quart. J. Mech. Appl. Math. 61 (2) (2008) 181–203.

[65] D. Violeau, T. Fonty, Calculating the smoothing error in SPH, Comput. & Fluids 191 (2019) 104240.